nature physics

SUPPLEMENTARY INFORMATION

https://doi.org/10.1038/s41567-018-0358-7

In the format provided by the authors and unedited.

Guiding self-organized pattern formation in cell polarity establishment

Peter Gross[1,2,3,8], K. Vijay Kumar[3,4,8], Nathan W. Goehring[5,6], Justin S. Bois[7], Carsten Hoege[2], Frank Jülicher[3] and Stephan W. Grill[1,2,3]*

[1]BIOTEC, TU Dresden, Dresden, Germany. [2]Max Planck Institute of Molecular Cell Biology and Genetics, Dresden, Germany. [3]Max Planck Institute for the Physics of Complex Systems, Dresden, Germany. [4]International Centre for Theoretical Sciences, Tata Institute of Fundamental Research, Bengaluru, India. [5]The Francis Crick Institute, London, UK. [6]Medical Research Council Laboratory for Molecular Cell Biology, University College London, London, UK. [7]California Institute of Technology, Pasadena, CA, USA. [8]These authors contributed equally: Peter Gross, K. Vijay Kumar.
*e-mail: stephan.grill@tu-dresden.de

1 Supplementary Discussion

1.1 The effect of PAR proteins on NMY-2 is negligible during *par-2* and *par-6* double RNAi

We investigated the effect of the PAR proteins on NMY-2 concentrations during *par-2* and *par-6* double RNAi as follows. First we determined the reduction of PAR-2 and PAR-6 amounts, during *par-2* and *par-6* double RNAi and *par-6* RNAi (Supplementary Fig. 3n-q). We found that for *par-2* and *par-6* double RNAi, the total number of both proteins reduces down to approximately 30%, compared to the unperturbed condition. The decrease in PAR-6, part of the anterior PAR complex, which is the dominant NMY-2 regulator (Supplementary Fig. 2k), is more pronounced for *par-6* RNAi only (Supplementary Fig. 3n,p). We then compared the four parameters, obtained by fitting the NMY-2 concentration and flow profile, between the *par-2* and *par-6* double RNAi and the *par-6* RNAi condition. We observed that the four parameters changed only moderately, between both conditions (between 5% - 30%), (Supplementary Fig. 10). We furthermore compared the fit of the *par-2* and *par-6* double RNAi condition to a fit where we explicitly consider the experimentally measured surface concentration of PAR-2 and PAR-6, during *par-2* and *par-6* double RNAi. We fit the NMY-2 concentration profile and flow field, while explicitly considering how the PAR-6 concentration changes NMY-2 profiles, via the coupling constant k_{AM}. We observed that the four parameters changed between both conditions between 1% - 20% (Supplementary Fig. 11). We thus conclude that during *par-2* and *par-6* double RNAi, the PAR concentration fields can be neglected when describing the concentration fields of NMY-2 and its flow field.

1.2 The FRAP recovery time scale is identical to the NMY-2 dissociation rate

During the initial cortical flow phase, myosin locally exhibits pulsatory dynamics, with dynamic foci, structures of very high myosin concentrations (*1, 2*). This spatial and temporal inhomogeneity precludes a direct measurement of the NMY-2 dissociation rate with FRAP. We thus measure this quantity during the maintenance phase (t = 400s - 600s after polarity triggering), where myosin concentration is close to a steady state (Supplementary Fig. 2a,c), and extrapolate the measured dissociation rate to the cortical flow phase. The obtained spontaneous myosin dissociation rate is in good agreement with COMBI (co-moving mass balance imaging) measurements of myosin kinet-

ics in the flow phase (*2*), indicating that the binding kinetics of myosin do not change substantially during the early stage of the cell cycle.

1.2.1 Dynamical equations of the FRAP system

Consider a system of a membrane and a large cytoplasm. The concentration on the membrane is homogeneous and in a binding-unbinding equilibrium. The FRAP event happens in region S_2, while the region S_1 is not bleached. Also assume that the diffusivity of the molecule is small such that diffusive fluxes between the bleached and unbleached region can be neglected. This is actually the case for NMY-2, with its very low diffusion rate (Supplementary Table 2). In addition, we only analyze the central region of 6 X 6 μm of the bleached square of 9 X 9 μm to ensure that diffusion indeed does not matter for these experiments.
The fluorescent membrane concentration evolves by:

$$\partial_t c_1(t) = k_{on} c_{cyto}(t) - k_{off} c_1(t), \tag{1}$$

$$\partial_t c_2(t) = k_{on} c_{cyto}(t) - k_{off} c_2(t), \tag{2}$$

with $c_{cyto}(t)$, $c_1(t)$, and $c_2(t)$ the concentration of fluorescent particles in the cytoplasm, in region 1 and region 2 (the bleached region), respectively (see Supplementary Fig. 1a). k_{on} and k_{off} represent the equilibrium association and dissociation rates, respectively. The total number of particles is conserved:

$$N_{total} = const = N_{cyto} + N_1 + N_2, \tag{3}$$

with

$$N_{total} = V \cdot c_{cyto}(t) + S_1 \cdot c_1(t) + S_2 \cdot c_2(t), \tag{4}$$

such that (we use $\gamma = S_2/S_{tot}$ and $1-\gamma = S_1/S_{tot}$).

$$c_{cyto}(t) = \frac{N_{total}}{V} - \frac{S_1}{V} c_1(t) - \frac{S_2}{V} c_2(t) = \rho_{total} - \gamma\psi c_2(t) - (1-\gamma)\psi c_1(t); \tag{5}$$

Inserting this into eq. (1) and (2) results in:

$$\partial_t c_1(t) = k_{on}\rho_{total} - (1-\gamma)k_{on}\psi c_1(t) - \gamma k_{on}\psi c_2(t) - k_{off} c_1(t), \tag{6}$$

$$\partial_t c_2(t) = k_{on}\rho_{total} - (1-\gamma)k_{on}\psi c_1(t) - \gamma k_{on}\psi c_2(t) - k_{off} c_2(t), \tag{7}$$

This system of ordinary differential equations for c_1 and c_2 are thus coupled according to:

$$\partial_t \begin{pmatrix} c_1 \\ c_2 \end{pmatrix} = \begin{pmatrix} -k_{off} - (1-\gamma)k_{on}\psi & -\gamma k_{on}\psi \\ (\gamma-1)k_{on}\psi & -k_{off} - \gamma k_{on}\psi \end{pmatrix} \begin{pmatrix} c_1 \\ c_2 \end{pmatrix} + \begin{pmatrix} k_{on}\rho_{total} \\ k_{on}\rho_{total} \end{pmatrix} \tag{8}$$

With eigenvalues

$$\lambda_1 = -k_{off} - k_{on}\psi \tag{9}$$

$$\lambda_2 = -k_{off} \tag{10}$$

and the eigenvectors

$$e_1 = \begin{pmatrix} 1 \\ 1 \end{pmatrix} \tag{11}$$

$$e_2 = \begin{pmatrix} \frac{\gamma}{\gamma-1} \\ 1 \end{pmatrix} \tag{12}$$

1.2.2 Dynamics of the fluorescent population after the bleaching event

Let us only look at the fluorescent membrane concentration, after the FRAP event ($t = 0s$). For the initial condition, we assume that all molecules in the FRAP region are bleached and that outside of the FRAP region, the system is in binding-unbinding equilibrium. During the FRAP event, we bleach all molecules in region S_2. As initial conditions for the FRAP event, we assume that the concentration outside of the FRAP region is the equilibrium constant and inside the FRAP region it is zero:

$$c_1^o = \frac{k_{on}\rho_{total}}{k_{on}\psi + k_{off}}, \tag{13}$$

$$c_2^o = 0, \tag{14}$$

And the exact solution for this initial condition is:

$$\begin{pmatrix} c_1(t) \\ c_2(t) \end{pmatrix} = c_1^o \left[\gamma\left(\frac{\psi c_1^o}{\rho_{tot}} - 1\right) \begin{pmatrix} 1 \\ 1 \end{pmatrix} e^{-(k_{on}\psi + k_{off})t} + \begin{pmatrix} \gamma \\ \gamma - 1 \end{pmatrix} e^{-k_{off}t} + \left(1 - \gamma\frac{\psi}{\rho_{tot}}c_1^o\right) \begin{pmatrix} 1 \\ 1 \end{pmatrix} \right] \tag{15}$$

For small γ, the dynamics of the FRAP region ($c_2(t)$) is dominated by $e^{-k_{off}t}$, while the $e^{-(k_{on}\psi+k_{off})t}$ becomes increasingly important with increasing γ (Supplementary Fig. 1b,c). Numerical evaluations of the solution show that when the FRAP region is small compared to the total region, then the fluorescence recovery time-scale is in essence given by k_{off}. We use a FRAP region of 9 μm X 9 μm, which corresponds to a γ of about 0.02, and thus indeed in the region where k_{off} dominates the FRAP recovery time scale (Supplementary Fig. 1c).

2 Supplementary Equations

2.1 Model definition

We build a coarse-grained theory for the dynamics of the PAR-actomyosin system as follows. The sum total membrane-bound fraction, c, and the cytoplasmic fraction, c_{cyto}, of a protein c is a constant c_{tot}, throughout the polarity process (Supplementary Fig. 3i,j,l,m). Here c is either A, P or M. We write this constraint of limited protein pools as

$$c_{\text{tot}} = \oint_{\text{surface}} dS\, c + \int_{\text{cytoplasm}} dV\; c_{\text{cyto}}, \tag{16}$$

where dS and dV are surface and volume elements of the cell. For all the proteins involved (A,P,M), the cytoplasmic diffusion constants are much larger than their surface diffusion constants (*3*). As such, the cytoplasmic concentrations can be considered homogeneous. Within this approximation, the above equations for the number conservation take on the form

$$c_{\text{cyto}}(t) = \rho_c - \frac{1}{V}\oint_{\text{surface}} dS\, c(\mathbf{r},t) \tag{17}$$

where V is the total volume of the cell and $\rho_c = c_{\text{tot}}/V$, and $\mathbf{r}$ denotes a coordinate on the surface of the cell.

The spatiotemporal dynamics of the surface concentrations $c(\mathbf{r},t)$ are affected by three distinct physical processes: (i) surface transport by active hydrodynamic flows in the cortex, (ii) passive diffusive transport on the surface, and (iii) chemical reactions amongst the surface bound molecules and their cytoplasmic counterparts. As such, the transport equations take on the generic form

$$\partial_t c(\mathbf{r},t) = -\nabla\cdot(\mathbf{v}\,c) + D_c\nabla^2 c + R_c \tag{18}$$

where $\mathbf{v}(\mathbf{r},t)$ is the active hydrodynamic flow field in the actomyosin cortex, D_c is the diffusion constant, R_c represents the sum total of the reactions affecting c, and ∇ is a derivative operator on the cell surface. The hydrodynamics of the cortex is captured by a coarse-grained theory in which actomyosin activity generates active stresses in addition to the passive stresses (*4*). The total stress in a patch of the actomyosin cortex can be written as

$$\sigma_{\text{tot}} = \sigma_{\text{passive}} + \sigma_{\text{active}} \tag{19}$$

where σ_{passive} is the passive viscous stress arising in a hydrodynamic description of the cortex, and σ_{active} is the active stress arising from actomyosin activity. Neglecting inertia, the force-balance equation is

$$\nabla \cdot \sigma_{\text{tot}} = \gamma \mathbf{v} \tag{20}$$

where the term on the right-hand-side represents a simple frictional drag force on cortical flows due the surrounding cytoplasm/membrane (*4*). The active stress is up-regulated by the local concentration of NMY-2 like

$$\sigma_{\text{active}} = C_* \frac{M}{M + M_*}, \tag{21}$$

where C_* is the strength of contractility and M_* is a Hill coefficient. Any spatially inhomogeneous profile of myosin leads to an active stress, and gradients in this active stress generate flow (*4*).

2.2 Biochemical reactions

2.2.1 NMY-2 reactions

In addition to the turnover of the surface component of NMY-2 with the cytoplasmic component, the off-rate of NMY-2 was found to be regulated by the aPARs (Fig. 1c, main text). As such, the biochemical reactions that affect the surface NMY2 concentration can be written as

$$\tilde{R}_M = k_{\text{on},M} M_{\text{cyto}} - \left[k_{\text{off},M} - k_{AM} A\right] M \tag{22}$$

where $k_{\text{on},M}$ and $k_{\text{off},M}$ are the on- and off-rates to the cytoplasm, and k_{AM} is the coefficient of the regulation of the off-rate of NMY-2 by the anterior PARs. As evident from the above equation, the coupling k_{AM} cannot be arbitrarily large as this would make

the NMY-2 system unstable. However, as long as $\left[k_{\text{off},M} - k_{AM}\, A\right] > 0$, stability is ensured, a condition which was always met, in this study.

2.2.2 PAR reactions

The anterior and posterior PAR proteins have mutually antagonistic interaction between them (*5–9*). For the anterior PAR proteins, this antagonistic interaction occurs in the form of an on-rate regulation by the posterior PAR complex (*10, 11*), while for the posterior PAR complex, this realizes in the form of an off-rate regulation by the anterior PAR complex (*12*). Additionally, as discussed above, each PAR protein has a membrane-bound surface component and a cytoplasmic bulk component, with continuous exchange between these two components. Thus the biochemical interactions between the PAR proteins can be expressed as

$$R_A = \frac{k_{\text{on},A}}{(1 + k_{AP} P^{\alpha})} A_{\text{cyto}} - k_{\text{off},A}\, A \tag{23}$$

$$\tilde{R}_P = k_{\text{on},P}\, P_{\text{cyto}} - \left[k_{\text{off},P} + k_{PA}\, A^{\beta}\right] P \tag{24}$$

where $k_{\text{on},A}$ ($k_{\text{on},P}$) and $k_{\text{off},A}$ ($k_{\text{on},P}$) are the on- and off-rates of the anterior (posterior) PAR proteins, k_{AP} and k_{PA} are the coefficients of the mutually antagonistic interactions between them, and α, β are stoichiometric coefficients. This mutual antagonism between the PAR complexes leads to bistability in the possible states of the PAR system (*12–14*). Specifically, one finds that there are three main regions in the PAR parameters such that (i) only homogeneous PAR states are stable, (ii) only PAR domain states are stable, and (iii) stable states with homogeneous PAR profiles can coexist with PAR domain states that are also stable. In region (iii), a transition from the homogeneous state to the domain state require a non-uniform perturbation whose strength should exceed a certain magnitude in order to trigger transition into the domain state. This triggering of the self-organized state of the PAR system from the homogeneous state to the polarized domain state is guided by external cues arising from the centrosome.

2.3 Spatiotemporal cues that trigger the PAR system

The centrosome associated with the male pronucleus provides spatiotemporal cues that guide the PAR - actomyosin patterning process. The cues are spatially localized around the posterior pole, and act persistently for a finite period of time. Generally, the two guiding cues (PAR-2 stabilization cue, actomyosin cue) influence the PAR-actomyosin system via three interactions, with the actomyosin cue possessing two components:

1. PAR-2 stabilization cue: The microtubules associated with the centrosome lead to a reduction in the phosphorylation rate of PAR-2 (*15*). This ensures that the pPAR concentration locally rises, which in turn clears the aPARs and thus paves the way for the formation of a stable pPAR domain.

2. Myosin removal component of actomyosin cue: Through a yet undisclosed mechanism, the same centrosome locally depletes NMY-2 at the posterior pole (*16*) creating a spatial gradient in the cortical concentration NMY-2 (and hence the active stresses) which leads to cortical flows (Fig. 1a, main text). These flows clear out the anterior PARs, making way for the posterior PARs to nucleate a domain on the surface.

3. Contractility component of actomyosin cue: Additionally, NMY-2 contractility is up-regulated for a period of about 350s after triggering polarity establishment, by up-regulating RhoA, involving NOP-1 (*17*). By the end of the cortical flow period, cytoplasmic flows, which constrict the centrosome close to the actomyosin cortex at the posterior pole, also cease. Consequently, the timescale for which the centrosome remains in proximity to the actomyosin cortex and the timescale of actomyosin contractility is identical (Supplementary Fig. 5).

The above cues guide the PAR system to a proper polarized state starting from the homogeneous state. We note that the guiding-cue interactions (1) and (2), promoted by the centrosome (i) are localized in space near the posterior pole, (ii) gradually switch on when the centrosome approaches the posterior pole, and (iii) are 'on' for a finite time. With these considerations, we mathematically represent all three external cues by

$$\mathrm{c_P}(\mathbf{r},\mathrm{t}) = k_{PA} A^{\beta} P\, \kappa_P\, F_P(\mathbf{r})\, f_P(t), \tag{25}$$

$$\mathrm{c_{M1}}(\mathbf{r},\mathrm{t}) = -k_{\mathrm{off},M} M\, \kappa_M\, F_M(\mathbf{r})\, f_M(t), \tag{26}$$

$$\mathrm{c_{M2}}(\mathrm{t}) = f_C(t), \tag{27}$$

where κ_P and κ_M are the (dimensionless) strengths of the two cues. The functions $F_P(\mathbf{r})$ and $F_M(\mathbf{r})$ are localized near the posterior pole, and without loss of generality, we choose the a Gaussian functional form for their profiles

$$F_P(\mathbf{r}) = \exp\left(-\frac{(\mathbf{r}-\mathbf{r}_{\mathrm{posterior}})^2}{d_P^2}\right), \tag{28}$$

$$F_M(\mathbf{r}) = \exp\left(-\frac{(\mathbf{r}-\mathbf{r}_{\mathrm{posterior}})^2}{d_M^2}\right), \tag{29}$$

where $\mathbf{r}_{\text{posterior}}$ is the location of the posterior pole, d_P and d_M are the characteristic widths of the spatial profiles. Temporally, the PAR-2 stabilization cue and the myosin removal component of actomyosin cue switch on gradually from the off state, and persistently stay in the on-state for a finite time. The myosin removal cue component is active for a finite time and appears to switch off when the centrosome, attached to the male pronucleus detaches from the actomyosin cortex (Supplementary Fig. 5). Again, without loss of generality, we choose the following mathematical expression to describe temporal profile of the myosin removal cue component that switches on the trigger by transitioning from zero to one at $t = 0$ smoothly on the time scale $\tau_{M,\text{on}}$ and go back to zero after the time T_M, again smoothly on a time scale $\tau_{M,\text{off}}$:

$$f_M(t) = \frac{1}{2}\left[\tanh\left(\frac{t}{\tau_{M,\text{on}}}\right) - \tanh\left(\frac{t-T_M}{\tau_{M,\text{off}}}\right)\right]. \tag{30}$$

The PAR-2 stabilization cue is mediated by microtubules, emerging from the male pronucleus, which are in contact with the cortex even when the centrosome detaches from the cortex. Because of that, we describe the temporal profile of the PAR-2 stabilization cue by:

$$f_P(t) = \frac{1}{2}\left[\tanh\left(\frac{t}{\tau_{P,\text{on}}}\right) + 1\right], \tag{31}$$

which switches on the PAR-2 stabilization cue by transitioning from zero to one at $t = 0$ smoothly on the time scale $\tau_{P,\text{on}}$ and remaining on for the entire timescale of PAR polarity establishment. Since both the triggers arise from the same centrosome, the times at which the cues are turned 'on' are taken to be the same $t = 0$. The contractility cue component increases actomyosin contractility already before the centrosome provides the signal for polarity establishment, and decreases contractility at the same time that the centrosome leaves the proximity of the actomyosin cortex (Supplementary Fig. 5). We thus use the following temporal profile to describe the contractility cue:

$$f_C(t) = \frac{1}{2}\left[1 - \tanh\left(\frac{t-T_M}{\tau_{M,\text{off}}}\right)\right], \tag{32}$$

Note that the specific spatiotemporal profiles that we have chosen for the cues are generic. Other smooth forms are possible and would not lead to very different dynamics.

2.4 Complete model

With the considerations of the previous two sections, we can now write down the full set of biochemical reactions that govern the dynamics of A, P and M. They are

$$R_A = \frac{k_{\text{on},A}}{(1+k_{AP}P^{\alpha})} A_{\text{cyto}} - k_{\text{off},A}\, A, \tag{33}$$

$$R_P = k_{\text{on},P} P_{\text{cyto}} - \Big(k_{\text{off},P} + k_{PA} A^{\beta} \left[1 - \kappa_P\, F_P(\mathbf{r})\, f_P(t)\right] \Big) P, \tag{34}$$

$$R_M = k_{\text{on},M} M_{\text{cyto}} - \Big(k_{\text{off},M} \left[1 + \kappa_M\, F_M(\mathbf{r})\, f_M(t)\right] - k_{AM}\, A \Big) M. \tag{35}$$

Our experimental data is acquired in the mid-plane imaging geometry of the embryo. Assuming the entire polarization process has azimuthal symmetry about the anteroposterior axis of the embryo (*18*), we can simplify our theory by writing the dynamical equations in an elliptical cross-section of the embryo. This naturally leads us to consider periodic boundary conditions along the one-dimensional domain. Further, we neglect the curvature of the embryo (*12*) and finally consider our model on a one-dimensional line of size L with periodic boundary conditions.

The cytoplasmic concentration of a protein c (either A, P or M) in this one-dimensional theory is calculated from

$$c_{\text{cyto}} = c_{\text{tot}} - \frac{\psi}{L} \int_{-L/2}^{L/2} c(x,t)\, dx, \tag{36}$$

where ψ is the surface-to-volume ratio for the ellipsoidal geometry of the embryo, and $x \in [-L/2, L/2]$ with $x = 0$ corresponding to the posterior pole.

The total stress in the actomyosin cortex is given by

$$\sigma_{\text{tot}} = \eta\, \partial_x v + C_*\, f_C(t)\, \frac{M}{M+M_*}. \tag{37}$$

where η is the viscosity of the cortex (*4*). This together with the force-balance equation $\partial_x \sigma_{\text{tot}} = \gamma v$ leads to an equation for the cortical flows

$$\eta\, \partial_x^2 v - \gamma v = -C_*\, f_C(t)\, \partial_x \left(\frac{M}{M+M_*} \right). \tag{38}$$

Finally, the transport equations for A, P and M simplify to

$$\partial_t A = -\partial_x(vA) + D_A\partial_x^2 A + \frac{k_{\text{on},A}}{(1+k_{AP}P^\alpha)}A_{\text{cyto}} - k_{\text{off},A}\,A, \tag{39}$$

$$\partial_t P = -\partial_x(vP) + D_P\partial_x^2 P + k_{\text{on},P}P_{\text{cyto}} - \Big(k_{\text{off},P} + k_{PA}A^\beta\ \big[1-\kappa_P\,F_P(\mathbf{r})\,f_P(t)\big]\Big)\,P, \tag{40}$$

$$\partial_t M = -\partial_x(vM) + D_M\partial_x^2 M + k_{\text{on},M}M_{\text{cyto}} - \Big(k_{\text{off},M}\big[1+\kappa_M\,F_M(\mathbf{r})\,f_M(t)\big] - k_{AM}\,A\Big)\,M, \tag{41}$$

with

$$A_{\text{cyto}} = A_{\text{tot}} - \frac{\psi}{L}\int_{-L/2}^{L/2}dx A,\ P_{\text{cyto}} = P_{\text{tot}} - \frac{\psi}{L}\int_{-L/2}^{L/2}dx P,\ M_{\text{cyto}} = M_{\text{tot}} - \frac{\psi}{L}\int_{-L/2}^{L/2}dx M \tag{42}$$

and

$$F_P(x) = \exp\left(-\frac{x^2}{d_P^2}\right), \quad F_M(x) = \exp\left(-\frac{x^2}{d_M^2}\right), \tag{43}$$

$$f_P(t) = \frac{1}{2}\left[\tanh\left(\frac{t}{\tau_{P,\text{on}}}\right)+1\right], \tag{44}$$

$$f_M(t) = \frac{1}{2}\left[\tanh\left(\frac{t}{\tau_{M,\text{on}}}\right)-\tanh\left(\frac{t-T_M}{\tau_{M,\text{off}}}\right)\right], \tag{45}$$

$$f_C(t) = \frac{1}{2}\left[1-\tanh\left(\frac{t-T_M}{\tau_{M,\text{off}}}\right)\right]. \tag{46}$$

The above three transport equations (39, 40, 41) and the equation for the cortical flows (38) constitute our complete and self-consistent theory for PAR polarity in *C. elegans* embryos.

2.5 Numerical solutions of the model

Our theory as expressed by equations (38-46) cannot be solved analytically for the spatiotemporal evolution of the dynamical fields, even in the simplified one-dimensional geometry. As such, we resort to numerical methods to solve the partial differential equations.

We set up the problem in a one-dimensional line of size L in a periodic geometry. The position coordinate $x \in [-L/2, L/2]$ with the point $x = 0$ corresponding to the location of the posterior pole. The periodic boundary conditions, implied by as-

suming azimuthal symmetry and midplane imaging, leads us to solving the cortical flow equation (38) with high-precision spectral methods (*19*). We then discretize the transport equations (39, 40, 41) with finite-difference methods and use the method of lines employing accurate high-order time-marching algorithms to solve the resulting equations (*20*), using custom built code in Python (*21*).

2.6 Parameter inference procedure

At first sight, it appears that our theory has a large number of adjustable parameters. However, the values for many parameters are well known in the literature. Our data analysis procedures described in the Methods sections have led us to infer several more parameters. As such, there are only a moderate number of parameters which are unknown. See Supplementary Table S2 for a list of the known and unknown parameters. The main parameters that are unknown are those that pertain the characteristics of the triggering cues. Fortunately, the modularity of the PAR - actomyosin system allows us to determine these parameters, few at a time, in a systematic manner.

- *mlc-4* RNAi allows us to decouple the PAR patterning system from the NMY-2-flow system. This allows us to determine the parameters of the PAR-2 stabilization cue and the strengths of the mutual antagonistic interactions between the PARs.
- The *par-2* and *par-6* double RNAi condition isolates the NMY-2-flow system, thus allowing us to infer the characteristics of the myosin removal and contractility cue component.

For each of these two modular subsystems, we employ a systematic procedure to infer the set of unknown parameters, as described below.

2.6.1 Comparing theory and experimental data

For a given set of model parameters, our numeric evaluation returns the spatiotemporal profiles of the three concentration fields and the cortical velocity field, at any required space-time resolution. However, for a nonlinear theory, such as the present one, there is no direct and simple way to compare the theoretical solutions with experimental data to assess how good a given parameter set is. The standard reduced chi-squared measure can lead to erroneous results (*22*). As such, we used the following procedure to assess the agreement between the experimental data and the theoretical solution for a given set of input parameters.

Condition	Theoretical description
mlc-4 RNAi	$\partial_t A = -\partial_x(vA) + D_A\partial_x^2 A + \frac{k_{\text{on},A}}{(1+k_{AP}P^\alpha)}A_{\text{cyto}} - k_{\text{off},A}A,$ $\partial_t P = -\partial_x(vP) + D_P\partial_x^2 P + k_{\text{on},P}P_{\text{cyto}} - \left(k_{\text{off},P} + k_{PA}A^\beta\left[1-\kappa_P F_P(\mathbf{r})\, f_P(t)\right]\right)P,$ $\partial_t M = -\partial_x(vM) + D_M\partial_x^2 M + k_{\text{on},M}M_{\text{cyto}} - \left(k_{\text{off},M}\left[1+\kappa_M F_M(\mathbf{r})\, f_M(t)\right] - k_{AM}A\right)M,$ $\eta\partial_x^2 v - \gamma v = -C_*\, f_C(t)\,\partial_x\left(\frac{M}{M+M_*}\right)$
par-2 + *par-6* RNAi	$\partial_t A = -\partial_x(vA) + D_A\partial_x^2 A + \frac{k_{\text{on},A}}{(1+k_{AP}P^\alpha)}A_{\text{cyto}} - k_{\text{off},A}A,$ $\partial_t P = -\partial_x(vP) + D_P\partial_x^2 P + k_{\text{on},P}P_{\text{cyto}} - \left(k_{\text{off},P} + k_{PA}A^\beta\left[1-\kappa_P F_P(\mathbf{r})\, f_P(t)\right]\right)P,$ $\partial_t M = -\partial_x(vM) + D_M\partial_x^2 M + k_{\text{on},M}M_{\text{cyto}} - \left(k_{\text{off},M}\left[1+\kappa_M F_M(\mathbf{r})\, f_M(t)\right] - k_{AM}A\right)M,$ $\eta\partial_x^2 v - \gamma v = -C_*\, f_C(t)\,\partial_x\left(\frac{M}{M+M_*}\right)$
wt-MT$^-$	$\partial_t A = -\partial_x(vA) + D_A\partial_x^2 A + \frac{k_{\text{on},A}}{(1+k_{AP}P^\alpha)}A_{\text{cyto}} - k_{\text{off},A}A,$ $\partial_t P = -\partial_x(vP) + D_P\partial_x^2 P + k_{\text{on},P}P_{\text{cyto}} - \left(k_{\text{off},P} + k_{PA}A^\beta\left[1-\kappa_P F_P(\mathbf{r})\, f_P(t)\right]\right)P,$ $\partial_t M = -\partial_x(vM) + D_M\partial_x^2 M + k_{\text{on},M}M_{\text{cyto}} - \left(k_{\text{off},M}\left[1+\kappa_M F_M(\mathbf{r})\, f_M(t)\right] - k_{AM}A\right)M,$ $\eta\partial_x^2 v - \gamma v = -C_*\, f_C(t)\,\partial_x\left(\frac{M}{M+M_*}\right)$
unperturbed	$\partial_t A = -\partial_x(vA) + D_A\partial_x^2 A + \frac{k_{\text{on},A}}{(1+k_{AP}P^\alpha)}A_{\text{cyto}} - k_{\text{off},A}A,$ $\partial_t P = -\partial_x(vP) + D_P\partial_x^2 P + k_{\text{on},P}P_{\text{cyto}} - \left(k_{\text{off},P} + k_{PA}A^\beta\left[1-\kappa_P F_P(\mathbf{r})\, f_P(t)\right]\right)P,$ $\partial_t M = -\partial_x(vM) + D_M\partial_x^2 M + k_{\text{on},M}M_{\text{cyto}} - \left(k_{\text{off},M}\left[1+\kappa_M F_M(\mathbf{r})\, f_M(t)\right] - k_{AM}A\right)M,$ $\eta\partial_x^2 v - \gamma v = -C_*\, f_C(t)\,\partial_x\left(\frac{M}{M+M_*}\right)$

Table S1 – Table showing the equations used for different conditions.

- The experimental data fields $A_{\text{expt}}(x,t)$, $P_{\text{expt}}(x,t)$, $M_{\text{expt}}(x,t)$ and $v_{\text{expt}}(x,t)$ are arrays of shape $n_{\text{space}} \times n_{\text{time}}$ (Fig. 3a-c, h-j, main text). The theoretical solutions, $A_{\text{theory}}(x,t)$, $P_{\text{theory}}(x,t)$, $M_{\text{theory}}(x,t)$ and $v_{\text{theory}}(x,t)$, are also obtained at the same space-time resolution.

- We then order the space-time points in a sequence and compute the normalized residual array

$$\mathscr{R}_Z = \{\frac{Z_{\text{expt}}(x,t) - Z_{\text{theory}}(x,t)}{\sigma_{\text{expt}}(x,t)} \mid x,t\}, \qquad Z = \{A,P,M,v\} \tag{47}$$

  where $\sigma_{\text{expt}}(x,t)$ is the experimental standard error of the mean for the variable Z at the point (x,t). Note that for each field Z, the array $\mathscr{R}_Z$ is a one-dimensional vector of length $n_{\text{space}} \times n_{\text{time}}$.

- For multiple fields, we collate the residual arrays into a single residual array $\mathscr{R} = \{\mathscr{R}_A, \mathscr{R}_P, \mathscr{R}_M, \mathscr{R}_v\}$.

- If the deviation of the data from the theoretical model is entirely due to statistical fluctuations, then the array $\mathscr{R}$ should have a normal distribution with zero mean and unit variance. We thus calculate, for each condition the two quantities (mean: $\mathscr{R}_{\text{mean}}$, variance: $\mathscr{R}_{\text{variance}}$) to characterize the goodness of the fit.

- As a goodness of fit test, we compare the normalized histogram of the array $\mathscr{R}$ with a normal distribution. To get a quantitative estimate of the comparison, we generate the quantile plots for the residual array $\mathscr{R}$ against a standard normal distribution. In the ideal case, this plot would be a straight line with unit slope and zero intercept (Supplementary Fig. 14).

In order to obtain good estimates of the four parameters ($k_{\text{on},A}, k_{\text{on},P}, k_{AP}, k_{PA}$) of the non-linear PAR reaction network and the strength of the PAR-2 stabilization cue (κ_P), we applied a fitting procedure where we first systematically evaluated a cost function, which quantifies the agreement of the theoretical solution with the experimental data, over a large range of parameter values. We systematically explored a broad range of combinations of the 5 parameters and compared the theoretical solution to the experimental data. For this comparison, we used the cost function

$$\text{cost} = \ (\mathscr{R}_{\text{variance}} - 1) \ + \ |\mathscr{R}_{\text{mean}}|, \tag{48}$$

for which each term is zero when the deviation of the data from the theoretical model is entirely due to statistical fluctuations. We evaluated the cost function for both, of the *mlc-4* RNAi condition and the PAR-2 MT- condition. For the *mlc-4* RNAi condition, flows are inhibited, while for the PAR-2 MT- condition, the PAR-2 stabilization cue is inhibited, such that both conditions provide relatively simple cases that cover a broad spectrum of phenotypes. To obtain a good estimate for $k_{\text{on},A}, k_{\text{on},P}, k_{AP}, k_{PA}$ and κ_P, we used:

$$\text{cost} = \ \frac{1}{2}(\text{cost}_{mlc4} + \text{cost}_{\text{PAR2MT}-}). \tag{49}$$

For each condition, we focused on parameter regions in which the homogeneous A-high state is stable (evaluated by linear stability analysis) and the PAR biochemistry shows multistability (the P and A nullclines have more than one intersection point). For instance, Supplementary Fig. 13 shows a heat map of this cost function for the *mlc-4* RNAi condition in some plane. We determined the global minimum of the cost function over this grid of 5 parameters to obtain an optimal starting parameter set. This parameter set, in combination with estimates for the width d_P and the switching time

$\tau_{P,\mathrm{on}}$ was then used as a starting point for a least squares minimization procedure using the Levenberg-Marquardt fitting algorithm. For the NMY-2-flow system, only 4 parameters were unknown (Supplemental Table S2 andS3) and for good convergence it was sufficient to use manual estimates as starting values for the least squares minimization procedure using the Levenberg-Marquardt fitting algorithm. We used the python library 'lmfit' to perform this final stage of the fitting procedure (*23*). This procedure also gives us estimates of the uncertainties (1σ) in the inferred parameters, from which we calculate and report the 95% confidence intervals. Note, however, that the estimates of the 95% confidence intervals from such a fitting procedure are generally not very robust and should be treated with caution (*22*).

2.6.2 Sensitivity analysis

We used a one-variable-at-a-time method to evaluate the sensitivity of our model solution to changes in the values of all parameters. For that, we varied one of our model parameters, while keeping the other parameters fixed to the values in Supplementary Table S2. We increased as well as decreased each parameter value. Then we evaluated the change in the solution by the following distance function. Let A_0, P_0, M_0 and v_0 be the solutions for the unperturbed condition. Let $A_{h/l}, P_{h/l}, M_{h/l}$ and $v_{h/l}$ be the concentration and flow fields for the variation of one parameter (high or low).
Then we define the distance measure for the unperturbed condition as:

$$\frac{1}{4}\Big(\frac{\int_{x,t}(A_0-A_{h/l})^2dxdt}{\int_{x,t}A_0^2dxdt}+\frac{\int_{x,t}(P_0-P_{h/l})^2dxdt}{\int_{x,t}P_0^2dxdt}+\frac{\int_{x,t}(M_0-M_{h/l})^2dxdt}{\int_{x,t}M_0^2dxdt}+\frac{\int_{x,t}(v_0-v_{h/l})^2dxdt}{\int_{x,t}v_0^2dxdt}\Big) \quad (50)$$

The distance value is zero for identical concentration fields in A, P and M and flow fields v. The distance is expressed as variance and normalized by the mean (Supplementary Fig. 12). We find that less than 30 percent of the parameters have a significant impact on the solutions. The most impactful parameters control the anterior PAR proteins and thus the stability of the initial, homogeneous state.

2.7 Linear stability analysis for the PAR-myosin-flow system

The PAR biochemical reactions represented by the equations (23) and (24) exhibit bistability for $\alpha \geq 1, \beta > 1$ or $\alpha > 1, \beta \geq 1$ (*12, 13*). For the best set of parameters determined for the unperturbed condition, the nullclines $R_A = 0$ and $\tilde{R}_P = 0$ defined by equation (23) and (24) have three possible solutions for the uniform steady-states of the PAR system, represented by three intersection points. It turns out that the aPAR domi-

nant state and the pPAR dominant state are stable, but the third state is unstable (*12, 13*). Additionally, the parameters corresponding the aPAR dominant state also allow the existence of polarized domain states, giving rise to coexistence of stable solutions. In the coexistence region, both the homogeneous state and the polarized domain state are stable to small fluctuations. A large perturbation, exceeding a certain threshold, is required to drive the system from the homogeneous state to the domain state. The *C. elegans* zygote is initially in the homogeneous aPAR dominant state and is driven by the cues to the polarized domain state. We next study the stability of the aPAR dominant homogeneous state to small non-uniform perturbations, in the presence of active mechanics, promoted by the NMY-2 concentration field.

We consider the PAR - actomyosin system without the external cues

$$\partial_t A = -\partial_x(vA) + D_A \partial_x^2 A + \frac{k_{\text{on},A}}{(1+k_{AP}P^\alpha)} A_{\text{cyto}} - k_{\text{off},A}\, A, \tag{51}$$

$$\partial_t P = -\partial_x(vP) + D_P \partial_x^2 P + k_{\text{on},P} P_{\text{cyto}} - \left(k_{\text{off},P} + k_{PA} A^\beta\right) P, \tag{52}$$

$$\partial_t M = -\partial_x(vM) + D_M \partial_x^2 M + k_{\text{on},M} M_{\text{cyto}} - \left(k_{\text{off},M} - k_{AM}\, A\right) M, \tag{53}$$

$$\eta\, \partial_x^2 v - \gamma v = -C_*\, \partial_x \left(\frac{M}{M+M_*}\right). \tag{54}$$

and investigate the stability of the homogeneous state with respect to small perturbations in the concentrations of the PARs and myosin. The above equations have a unique homogeneous steady-state, $\mathbf{c}_0 = (A_0, P_0, M_0)$, which is obtained by solving the following equations in a self-consistent manner:

$$A_0 = \frac{k_{\text{on},A}\, A_{\text{tot}}}{k_{\text{on},A}\, \psi + k_{\text{off},A} + k_{AP}\, P_0^\alpha}, \tag{55}$$

$$P_0 = \frac{k_{\text{on},P}\, P_{\text{tot}}}{k_{\text{on},P}\, \psi + k_{\text{off},P} + k_{PA}\, A_0^\beta}, \tag{56}$$

$$M_0 = \frac{k_{\text{on},M}\, M_{\text{tot}}}{k_{\text{on},M}\, \psi + k_{\text{off},M} - k_{AM} A_0}. \tag{57}$$

Following (*24*), the linear stability matrix, for a perturbation of the form e^{iqx} around the homogeneous steady-state $\mathbf{c}_0$, is

$$\mathscr{A}_{ij} = -q^2 D_i\, \delta_{ij} + C_* \frac{q^2}{1+q^2\ell^2}\; c_{i,0}\, \partial_{c_j} f(\mathbf{c}_0) + \partial_{c_j} R_i(\mathbf{c}_0) \tag{58}$$

where $i = \{A, P, M\}$. We get

$$\mathscr{A} = -q^2 \begin{pmatrix} D_A & 0 & 0 \\ 0 & D_P & 0 \\ 0 & 0 & D_M \end{pmatrix} \quad + \quad C_* \frac{q^2}{1+q^2\ell^2} \frac{M_*}{(M_0+M_*)^2} \begin{pmatrix} 0 & 0 & A_0 \\ 0 & 0 & P_0 \\ 0 & 0 & M_0 \end{pmatrix}$$

$$+ \begin{pmatrix} -k_{\mathrm{off},A} - \frac{\psi k_{\mathrm{on},A}\delta_{q,0}}{(1+k_{AP}P_0^\alpha)} & -\frac{k_{\mathrm{on},A}(A_{\mathrm{tot}} - \psi A_0 \delta_{q,0})}{(1+k_{AP}P_0^\alpha)^2}\, \alpha k_{AP} P_0^{\alpha-1} & 0 \\ -\beta k_{PA} A_0^{\beta-1} P_0 & -k_{\mathrm{off},P} - \psi k_{\mathrm{on},P}\delta_{q,0} - k_{PA}A_0^\beta & 0 \\ k_{AM} M_0 & 0 & -k_{\mathrm{off},M} - \psi k_{\mathrm{on},M}\delta_{q,0} - k_{AM}A_0 \end{pmatrix} \tag{59}$$

The eigenvalues of the above linear stability matrix determine whether the homogeneous state is stable to a small non-uniform perturbation. We numerically compute the eigenvalues using the best-fit parameters for the unperturbed condition (Table S2), and plot it as a function of the wavenumber q of the perturbation. If the eigenvalues for all spatial modes are smaller than zero, the homogeneous aPAR dominated state is stable. For Fig. 4b, main text, we explored a large range of values for k_{AM} and C_* and evaluated if the corresponding eigenvalues for all spatial modes of infinitesimally small perturbations remained negative. This then represents the region where the homogeneous state is stable. We furthermore simulated the PAR - actomyosin system, using the unperturbed-condition parameters, while k_{AM} and C_* were varied. As shown in Fig. 2b, main text, the PAR-2 stabilization cue causes PAR domain formation even in the absence of cortical flows. In order to investigate the perturbation originating from cortical flows, in their propensity to trigger domain formation, we numerically inactivated the PAR-2 stabilization cue by setting κ_P to zero. We then numerically evaluated if the perturbation of cortical flows triggers domain formation. In Fig. 4b, main text, the grey region indicates the parameter range, for which the advective polarity trigger fails to establish PAR domains.

2.8 Correlations in the concentration fields

In Supplementary Fig. 15, we plot the spatiotemporal normalized crosscorrelation functions (*25*) for the concentration fields of PAR-2, PAR-6 and NMY-2. The correlations obtained from the experimental data show negative correlation between PAR-2 and PAR-6 as well as NMY-2 and PAR-2 in the domain region and positive correlation between NMY-2 and PAR-6. For the parameter values of the unperturbed condition (Supplementary Table S2,S3), we plotted the correlation functions predicted from our

theory of guided mechanochemical self-organization. From this comparison it becomes evident that the agreement between theory and experiment is reasonably good, even at the quantitative level. Our mechanochemical theory of guided self-organization is a coarse-grained description of the microscopic dynamics. We have not included any stochastic fluctuations in our equations for the dynamics of the concentration fields, as coarse-grained theories average out stochastic fluctuations. The experimental *C. elegans* zygote of course exhibits stochastic fluctuations arising from various sources. Despite this fact, the correlation functions computed from experimental and the theoretical predictions still agree with each very well. This indicates that our theory is able to capture the dynamics of the system even beyond the simple mean-field level.

3 Supplementary Tables

parameter	known?	source	value
$k_{\text{on},A}$	x	fitting$^{(*)}$	$(2.115\pm0.008)\cdot10^{-2}\ \mu m s^{-1}$
$k_{\text{off},A}$	✓	(*10*)	$(9.2\pm2)\ \cdot10^{-3}s^{-1}$
$k_{\text{on},P}$	x	fitting$^{(*)}$	$(1.3012\pm0.0006)\cdot10^{-1}\mu m s^{-1}$
$k_{\text{off},P}$	✓	(*3*)	$(7.3\pm5.7)\cdot10^{-3}s^{-1}$
$k_{\text{on},M}$	✓	Fig. 1d	$0.199\pm0.04\mu m s^{-1}$
$k_{\text{off},M}$	✓	Fig. 1c	$0.117\pm0.009s^{-1}$
D_A	✓	(*10*)	$0.095\pm0.04\mu m^2 s^{-1}$
D_P	✓	(*3*)	$0.15\pm0.03\mu m^2 s^{-1}$
D_M	✓	Supplementary Fig. 4c	$0.054\pm0.003\mu m^2 s^{-1}$
ρ_A	✓	MACE, Supplementary Fig. 3i,j,l,m	see table S3
ρ_P	✓	MACE, Supplementary Fig. 3i,j,l,m	see table S3
ρ_M	✓	MACE, Supplementary Fig. 3i,j,l,m	see table S3
k_{PA}	x	fitting$^{(*)}$	$(1.318\pm0.0007)\cdot10^{-2}\mu m^4 s^{-1}$
k_{AP}	x	fitting$^{(*)}$	$1.11\pm0.017\mu m^2$
α	✓	(*12*)	1
β	✓	(*12*)	2
k_{AM}	✓	Fig. 1c	-$(2.0\pm0.7)\ \cdot10^{-3}\mu m^2 s^{-1}$
l	✓	(*26*)	$13.6\pm2.9\mu m$
C_*/γ	x	fitting$^{(*)}$	$10.4\pm\ 1.0Nm$
M_*	x	fitting$^{(*)}$	$8.0\pm\ 4.9\ \mu\text{m}^{-2}$
κ_M	x	fitting$^{(*)}$	4.9 ± 0.3
d_M	x	fitting$^{(*)}$	$15.9\ \pm0.6\mu m$
T_M	✓	Supplementary Fig. 6	see table S3
$\tau_{M,\text{on}}$	✓	Supplementary Fig. 6	see table S3
$\tau_{M,\text{off}}$	✓	Supplementary Fig. 6	see table S3
κ_P	x	fitting$^{(*)}$	0.951 ± 0.0006
d_P	x	fitting$^{(*)}$	$28.6\pm0.16\mu m$
$\tau_{P,on}$	x	fitting$^{(*)}$	$74\pm4.4s$

Table S2 – Parameter values of the physical model for the dynamics of PAR polarity establishment. $^{(*)}$: Errors represent the 95% confidence interval. Note however that this can be an underestimation of the real error, due to the nature of the fitting routine (see SI section 2.6.1).

condition	$\rho_A\ [\mu m^{-3}]$	$\rho_P\ [\mu m^{-3}]$	$\rho_M\ [\mu m^{-3}]$	$\tau_{M,\mathrm{on}}\ [s]$	$\tau_{M,\mathrm{off}}\ [s]$	$T_M\ [s]$
unperturbed	9.18 ± 0.50	6.30 ± 0.40	13.1 ± 0.9	32 ± 10	89 ± 19	322 ± 11
par-2 par-6 RNAi	4.03 ± 0.15	2.14 ± 0.17	14.1 ± 0.8	36 ± 11	99 ± 18	204 ± 10
par-6 RNAi	2.8 ± 0.25	6.0 ± 0.35	11.8 ± 0.6	29 ± 14	100 ± 25	185 ± 14
mlc-4 RNAi	9.22 ± 0.50	4.95 ± 0.37	–	–	–	–
PAR-2 MT- mutant	8.71 ± 0.45	4.02 ± 0.22	15.6 ± 0.9	32 ± 14	112 ± 30	403 ± 17

Table S3 – Table of condition-dependent parameter-values. Errors represent the 95% confidence interval.

NMY-2 GFP	LP133	*nmy-2(cp8[NMY-2::GFP + unc-119(+)]) I; unc-119(ed3) III*
NMY-2 mKate2	LP229	*nmy-2(cp52[nmy-2::mkate2 + LoxP unc-119(+) LoxP]) I; unc-119(ed3) III*
PH-Domain mCherry	OD70	*ltIs44pAA173; [pie-1p-mCherry::PH(PLC1delta1) + unc-119(+)]*
PH-Domain GFP	OD58	*ltIs38[pAA1; pie-1::GFP::PH(PLC1delta1) + unc-119(+)]*
PAR-2 MT- GFP	JH2815	*unc-119(ed3); axIs1934[pFM035 gfp::par-2$^{RNAi-resistant}$ [R183-5A]]*
PAR-2 GFP	TH129	*unc-119(ed3)III; ddIs25[[pie-1p::GFP::F58B6.3;unc-119(+)]*
PAR-6 mCherry	TH110	*unc-119(ed3)III; ddIs26[mCherry::T26E3.3;unc-119(+)]*
NMY-2 GFP PH-Domain mCherry	SWG070	cross between LP133 and OD70
NMY-2 mKate2 PAR-2 MT- GFP	SWG021	cross between LP229 and JH2815
PAR-2 MT- GFP PAR-6 mCherry	SWG025	cross between JH2815 and TH110
PAR-2 GFP PAR-6 mCherry	TH120	cross between TH129 and TH110
PAR-2 mNeonGreen SPD-5 GFP	SWG142	cross between SWG143 and OD847

Table S4 – *C. elegans* strains, used in this study.

References

1. François B Robin, Jonathan B Michaux, William M McFadden, and Edwin M Munro. Excitable rhoa dynamics drive pulsed contractions in the early c. elegans embryo. *bioRxiv*, 2016.

2. Masatoshi Nishikawa, Sundar Ram Naganathan, Frank Juelicher, and Stephan W. Grill. Controlling contractile instabilities in the actomyosin cortex. *eLife*, 6, JAN 28 2017.

3. Nathan W. Goehring, Carsten Hoege, Stephan W. Grill, and Anthony A. Hyman. PAR proteins diffuse freely across the anterior-posterior boundary in polarized C. elegans embryos. *Journal of Cell Biology*, 193(3):583–594, MAY 2 2011.

4. Mirjam Mayer, Martin Depken, Justin S. Bois, Frank Juelicher, and Stephan W. Grill. Anisotropies in cortical tension reveal the physical basis of polarizing cortical flows. *Nature*, 467(7315):617–U150, SEP 2010.

5. Bob Goldstein and Ian G. Macara. The PAR proteins: Fundamental players in animal cell polarization. *Developmental Cell*, 13(5):609–622, NOV 2007.

6. B Etemadmoghadam, S Guo, and KJ Kemphues. Asymmetrically distributed PAR-3 protein contributes to cell polarity and spindle alignment in early *C. elegans* embryos. *Cell*, 83(5):743–752, DEC 1 1995.

7. L Boyd, S Guo, D Levitan, DT Stinchcomb, and KJ Kemphues. PAR-2 is asymmetrically distributed and promotes association of P granules and PAR-1 with the cortex in C. elegans embryos. *Development*, 122(10):3075–3084, OCT 1996.

8. R Benton and D St Johnston. Drosophila PAR-1 and 14-3-3 inhibit Bazooka/PAR-3 to establish complementary cortical domains in polarized cells. *Cell*, 115(6):691–704, DEC 12 2003.

9. YS Hao, L Boyd, and G Seydoux. Stabilization of cell polarity by the C. elegans RING protein PAR-2. *Developmental Cell*, 10(2):199–208, FEB 2006.

10. Francois B. Robin, William M. McFadden, Baixue Yao, and Edwin M. Munro. Single-molecule analysis of cell surface dynamics in Caenorhabditis elegans embryos. *Nature Methods*, 11(6):677+, JUN 2014.

11. Anne Sailer, Alexander Anneken, Younan Li, Sam Lee, and Edwin Munro. Dynamic Opposition of Clustered Proteins Stabilizes Cortical Polarity in the C. elegans Zygote. *Developmental Cell*, 35(1):131–142, OCT 12 2015.

12. Nathan W. Goehring, Philipp Khuc Trong, Justin S. Bois, Debanjan Chowdhury, Ernesto M. Nicola, Anthony A. Hyman, and Stephan W. Grill. Polarization of PAR Proteins by Advective Triggering of a Pattern-Forming System. *Science*, 334(6059):1137–1141, NOV 25 2011.

13. Philipp Khuc Trong, Ernesto M. Nicola, Nathan W. Goehring, K. Vijay Kumar, and Stephan W. Grill. Parameter-space topology of models for cell polarity. *New Journal Of Physics*, 16, JUN 13 2014.

14. Sungrim Seirin Lee and Tatsuo Shibata. Self-organization and advective transport in the cell polarity formation for asymmetric cell division. *Journal of Theoretical Biology*, 382:1–14, 2015.

15. Fumio Motegi, Seth Zonies, Yingsong Hao, Adrian A. Cuenca, Erik Griffin, and Geraldine Seydoux. Microtubules induce self-organization of polarized PAR domains in Caenorhabditis elegans zygotes. *Nature Cell Biology*, 13(11):1361–U171, 2011.

16. Fumio Motegi and Asako Sugimoto. Sequential functioning of the ECT-2 RhoGEF, RHO-1 and CDC-42 establishes cell polarity in Caenorhabditis elegans embryos. *Nature Cell Biology*, 8(9):978–U80, 2006.

17. Yu Chung Tse, Michael Werner, Katrina M. Longhini, Jean-Claude Labbe, Bob Goldstein, and Michael Glotzer. RhoA activation during polarization and cytokinesis of the early Caenorhabditis elegans embryo is differentially dependent on NOP-1 and CYK-4. *Molecular Biology of the Cell*, 23(20):4020–4031, 2012.

18. Lesilee Rose and Pierre Gönczy. Polarity establishment, asymmetric division and segregation of fate determinants in early C. elegans embryos. *WormBook*, pages 1–43, December 2014.

19. Lloyd N. Trefethen. *Spectral Methods in MATLAB (Software, Environments, Tools)*. SIAM: Society for Industrial and Applied Mathematics, 2 2001.

20. Willem Hundsdorfer and Jan G. Verwer. *Numerical Solutions of Time-Dependent Advection-Diffusion-Reaction Equations*. Springer, 2007.

21. Python software foundation. http://www.python.org.

22. R. Andrae, T. Schulze-Hartung, and P. Melchior. Dos and don'ts of reduced chi-squared. *ArXiv e-prints*, December 2010.

23. Matthew Newville, Till Stensitzki, Daniel B. Allen, and Antonino Ingargiola. LMFIT: Non-Linear Least-Square Minimization and Curve-Fitting for Python, September 2014.

24. Justin S. Bois, Frank Jülicher, and Stephan W. Grill. Pattern Formation in Active Fluids. *Physical Review Letters*, 106(2), 2011.

25. D Padfield. Masked Object Registration in the Fourier Domain. *IEEE Transactions on Image Processing*, 21(5):2706–2718, 2012.

26. Arnab Saha, Masatoshi Nishikawa, Martin Behrndt, Carl-Philipp Heisenberg, Frank Jülicher, and Stephan W. Grill. Determining Physical Properties of the Cell Cortex. *Biophysical Journal*, 110(6):1421–1429, 2016.

27. William Thielicke and Eize J. Stamhuis. PIVlab - Time-Resolved Digital Particle Image Velocimetry Tool for MATLAB. 07 2014.

Supplementary Movie Legends

Movie S1. Concentration field of PAR-2::GFP (blue, N = 8) and PAR-6::mCherry (red, N = 8), during *mlc-4* RNAi, over time. Error bands represent the standard error of the mean. The solid line shows the best fit, using equations as described in table S1, with parameters shown in tables S2 and S3.

Movie S2. Ensemble-averaged concentration field of NMY-2::GFP (grey, N = 8) and the ensemble-averaged NMY-2 flow field (green, N = 10), during *par-2* and *par-6* double RNAi, over time. Error bands represent the standard error of the mean. The solid line shows the best fit, using equations as described in table S1, with parameters shown in tables S2 and S3.

Movie S3. Ensemble-averaged concentration field of PAR-2-MT-::GFP (blue, N = 9) and PAR-6::mCherry (red, N = 9) NMY-2::mKate2 (grey, N = 6) and the ensemble-averaged NMY-2 flow field (green, N = 9) for the PAR-2 MT- condition, over time. Error bands represent the standard error of the mean. The solid line shows the model prediction, using equations as described in table S1, with parameters shown in tables S2 and S3.

Movie S4. Ensemble-averaged concentration field of PAR-2::GFP (blue, N = 6) and PAR-6::mCherry (red, N = 6) NMY-2::GFP (grey, N = 8) and the ensemble-averaged NMY-2 flow field (green, N = 12) for the unperturbed condition, over time. Error bands represent the standard error of the mean. The solid line shows the model prediction, using equations as described in table S1, with parameters shown in tables S2 and S3.

Movie S5. Ensemble-averaged concentration field of PAR-2::GFP (blue, N = 6) and PAR-6::mCherry (red, N = 6) NMY-2::GFP (grey, N = 8) and the ensemble-averaged NMY-2 flow field (green, N = 12) for the unperturbed condition, over time. Error bands represent the standard error of the mean. The solid line shows a fit to the model, using equations as described in table S1, as shown in Supplementary Fig. 9.

Supplementary Figures

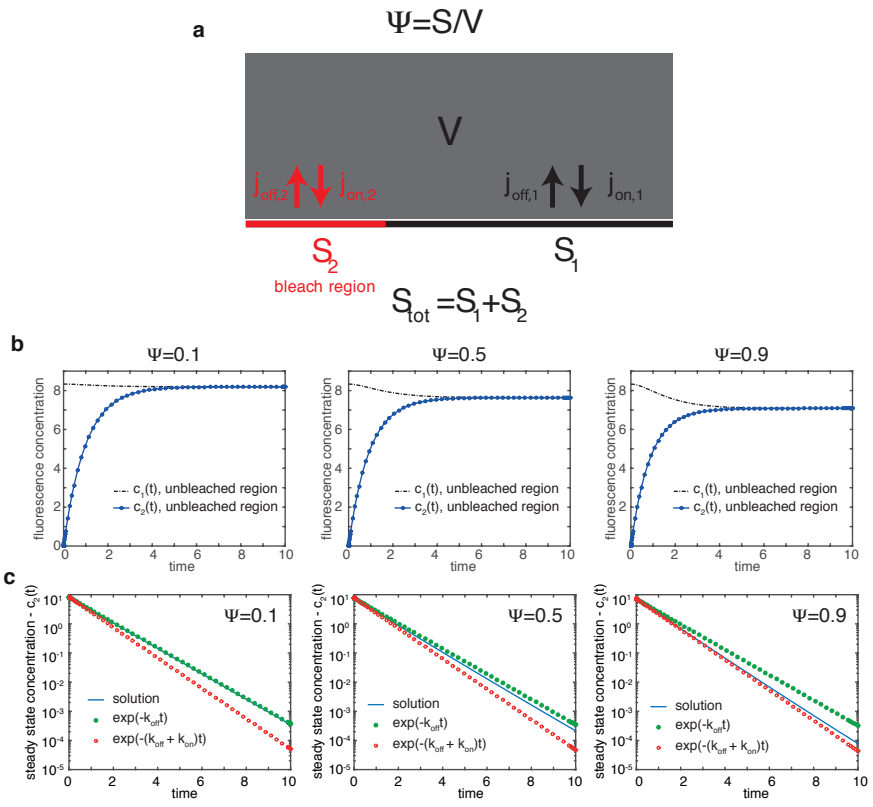

Fig. S1 – FRAP as method to measure dissociation rates. a, FRAP geometry. The membrane consists out of a region S_1, which is not bleached, and a region S_2, where the bleaching event has taken place. We consider $\gamma = S_2/S_{tot}$ as the fraction of the bleached to the total surface area. Both regions are coupled to the cytoplasm V. **b**, Concentrations of fluorescence particles on the membrane, after the FRAP event. First row: Dynamics of the concentration at the bleached region (blue, S2) and the unbleached region (black, S1) as a function of γ, which gives the ratio of the bleached region to the total surface area. Second row: The solution of the concentration of the bleached region minus the steady state, on a log plot, also for the three different γ values (0.1, 0.5, 0.9). Also plotted are the dynamics of the two eigenvalues, $\lambda_1 = -k_{off} - k_{on}\psi$ and $\lambda_2 = -k_{off}$, as a guide to the eye. All three conditions used: $k_{on} = 1$, $k_{off} = 1$, $\psi = 0.2$, $\rho_{total} = 10$.

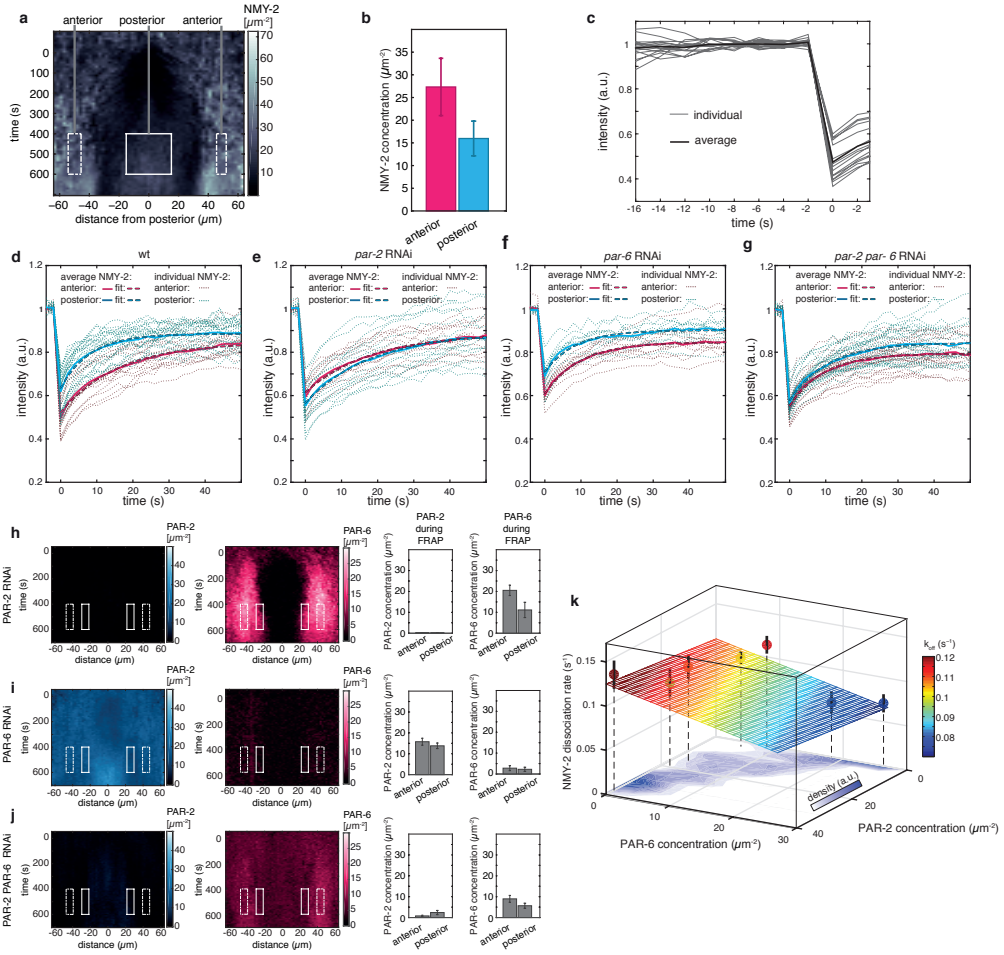
a
anterior
posterior
anterior
NMY-2 [μm⁻²]
time (s)
distance from posterior (μm)
b
NMY-2 concentration (μm⁻²)
anterior
posterior
c
intensity (a.u.)
individual
average
time (s)
d
wt
e
par-2 RNAi
f
par-6 RNAi
g
par-2 par- 6 RNAi
average NMY-2:
individual NMY-2:
anterior:
posterior:
fit:
intensity (a.u.)
time (s)
h
PAR-2 RNAi
PAR-6 [μm⁻²]
PAR-2 during FRAP
PAR-6 during FRAP
PAR-2 concentration (μm⁻²)
PAR-6 concentration (μm⁻²)
distance (μm)
i
PAR-6 RNAi
PAR-2 [μm⁻²]
j
PAR-2 PAR-6 RNAi
k
NMY-2 dissociation rate (s⁻¹)
PAR-6 concentration (μm⁻²)
PAR-2 concentration (μm⁻²)
density (a.u.)
k_off (s⁻¹)

Fig. S2 – NMY-2 dissociation rate as a function of the PAR concentration. **a**, Spatiotemporal concentration profile of NMY-2 (see Fig. 3i, main text, N=8) during fluorescence recovery after photobleaching (FRAP). FRAP was performed in a time period where the NMY-2 levels were close to steady state. To determine the average concentration of NMY-2 during the FRAP events, we calculated the mean and standard deviation in a time interval between 400s and 600s after polarity triggering. We defined the posterior region as an interval between -15 µm and 15 µm. The anterior region was defined as $\pm$ 45 µm to $\pm$ 55 µm. **b**, Average NMY-2 concentration and standard deviation in the anterior and posterior domain, using panel a (N=8). **c**, The NMY-2 concentration prior to the FRAP event reached a steady state (anterior, N=16). Light grey: individual NMY-2 concentrations. Dark grey: averaged NMY-2 concentration. Individual and averaged FRAP recovery of NMY-2 both in the anterior (red) and in the posterior (cyan) hemisphere, displayed for the four conditions: **d**, unperturbed (anterior: N=16, posterior: N=24), **e**, *par-2* RNAi (anterior: N=11, posterior: N=15), **f**, *par-6* RNAi (anterior: N=12, posterior: N=9), **g**, *par-2* + *par-6* RNAi (anterior: N=26, posterior: N=24). Fitting the fluorescence recovery provided the NMY-2 dissociation rates, shown in Fig. 1b, main text. Concentration of PAR proteins during FRAP experiments for various RNAi perturbations: spatiotemporal profile of PAR-2, PAR-6, as well as PAR-2 and PAR-6 concentration and standard deviation in the anterior (dashed rectangle) and posterior domain (rectangle) for **h**, *par-2* RNAi (N=7), **i**, *par-6* RNAi (N=6) and **j**, *par-2 par-6* double RNAi (N=10). The distance of the FRAP region to the posterior pole was determined prior to each individual FRAP event, yielding $d = 43.3\pm$ 2.6 µm for anterior FRAP and $d = 25.6\pm$ 2.8 µm for posterior FRAP, as average distance. **k**, NMY-2 dissociation rates, measured by FRAP (Fig. 1b,c, main text), plotted against the respective PAR-2 and PAR-6 concentrations. Error bars are standard error of the mean. Note that we excluded k_{diss} during *par-2* RNAi in the posterior domain, since small uncertainties in the FRAP position can have a strong impact on the PAR-6 concentration, which is thus difficult to asses. We fitted the dissociation rate with a linear relation $k_{\text{diss}} = k_{\text{off},M} + k_{AM}A + k_{PM}P$, and inferred $k_{AM} = -0.0016 \pm 0.0023$ µm^{2}s^{-1}, $k_{PM} = 3.6\text{e}-04 \pm 0.001.9$ µm^{2}s^{-1} and $k_{\text{off},M} = 0.16 \pm 0.002$ s^{-1}.

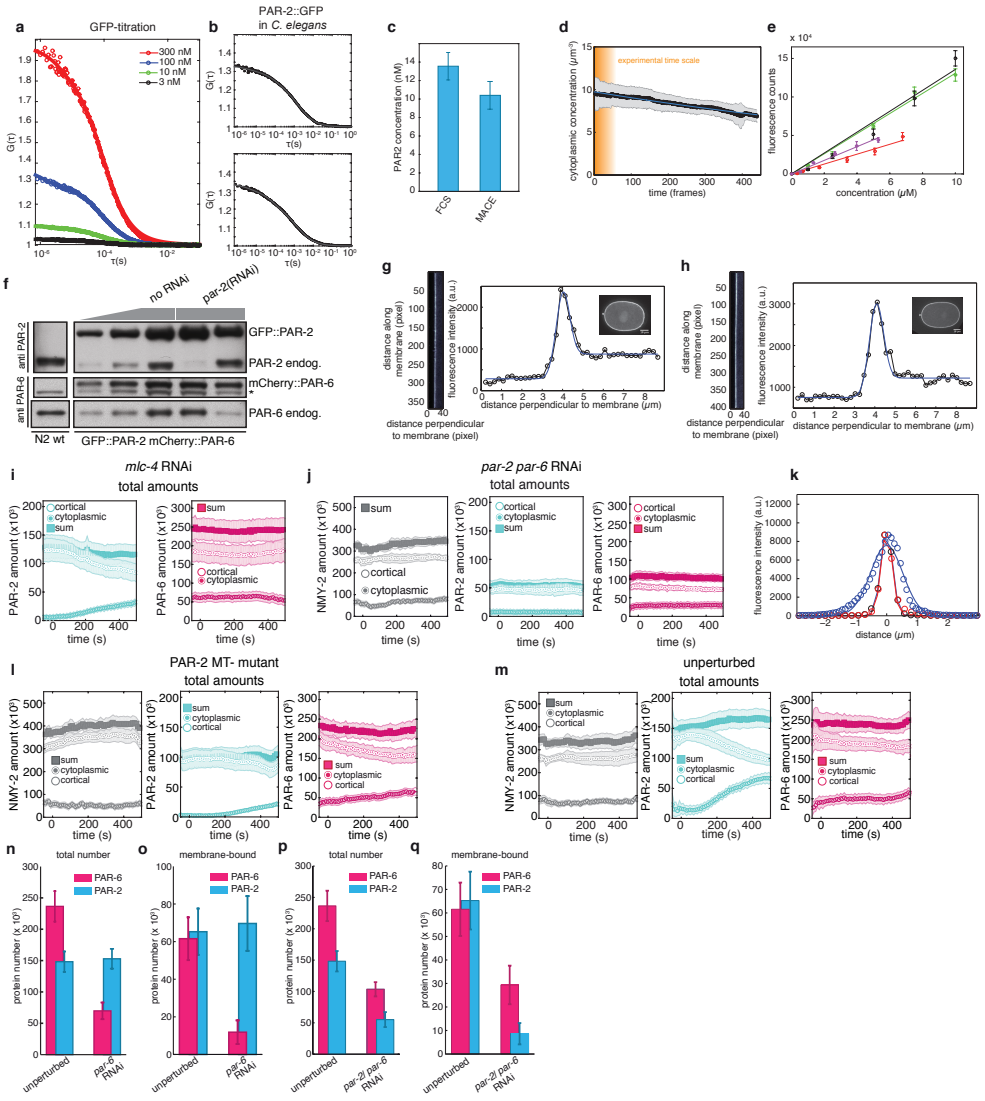
a
GFP-titration
300 nM
100 nM
10 nM
3 nM
G(τ)
τ(s)
b
PAR-2::GFP
in C. elegans
c
PAR2 concentration (nM)
FCS
MACE
d
experimental time scale
cytoplasmic concentration (μm⁻³)
time (frames)
e
x 10⁴
fluorescence counts
concentration (μM)
f
no RNAi
par-2(RNAi)
anti PAR-2
anti PAR-6
GFP::PAR-2
PAR-2 endog.
mCherry::PAR-6
*
PAR-6 endog.
N2 wt
GFP::PAR-2 mCherry::PAR-6
g
distance along membrane (pixel)
fluorescence intensity (a.u.)
distance perpendicular to membrane (μm)
distance perpendicular to membrane (pixel)
h
distance along membrane (pixel)
fluorescence intensity (a.u.)
distance perpendicular to membrane (μm)
distance perpendicular to membrane (pixel)
i
mlc-4 RNAi
total amounts
cortical
cytoplasmic
sum
PAR-2 amount (x10⁶)
PAR-6 amount (x10⁶)
time (s)
j
par-2 par-6 RNAi
total amounts
NMY-2 amount (x10⁶)
PAR-2 amount (x10⁶)
PAR-6 amount (x10⁶)
time (s)
k
fluorescence intensity (a.u.)
distance (μm)
l
PAR-2 MT- mutant
total amounts
NMY-2 amount (x10⁶)
PAR-2 amount (x10⁶)
PAR-6 amount (x10⁶)
time (s)
m
unperturbed
total amounts
NMY-2 amount (x10⁶)
PAR-2 amount (x10⁶)
PAR-6 amount (x10⁶)
time (s)
n
total number
PAR-6
PAR-2
protein number (x 10⁶)
unperturbed
par-6 RNAi
o
membrane-bound
PAR-6
PAR-2
protein number (x 10⁶)
unperturbed
par-6 RNAi
p
total number
PAR-6
PAR-2
protein number (x 10⁶)
unperturbed
par-2 par-6 RNAi
q
membrane-bound
PAR-6
PAR-2
protein number (x 10⁶)
unperturbed
par-2 par-6 RNAi

Fig. S3 – Protein concentrations measured by MACE. a, FCS autocorrelation spectra for GFP in solution, with 4 different concentrations (300 nM, 100 nM, 10 nM, 3 nM). Quantitative analysis yielded $V_{\mathrm{conf}} = 3.3e^{-16} \pm 3e^{-17}$ liters. **b**, Two individual FCS autocorrelation spectra for PAR-2::GFP in living *C. elegans* zygotes (circles). Black line: Theoretical fit, yielding a diffusive time-scale of $\tau_D = 98.5$ μs and $\tau_D = 77.5$ μs. **c**, Comparing the PAR-2 concentration of *C. elegans* one-cell zygotes, determined via FCS (13.6 ± 1.5 nM, N=21) with the quantity determined via MACE (10.4 ± 1.5 nM, N=8). **d**, Photobleaching during image-acquisition, for cytoplasmic NMY-2::GFP concentration (N=6) Error: Standard deviation. Blue line: exponential fit yielding a bleaching time scale of t_{bleach} = 1428 frames. **e:** Fluorescence calibration curves of GFP (green), mCherry (red), mNeonGreen (magenta) and mKate2 (black). Error bars: Standard deviation. The solid line shows a linear fit (see Methods). **f**, The ratio of labeled to unlabelled PAR-2 and PAR-6. Left side: Western blot against PAR-2 and PAR-6 for the N2 wt line. Right side: Western blot against PAR-2 and PAR-6 for the PAR-2::GFP and PAR-6::mCherry transgenic line. The asterisk marks a non-specific band close to PAR-6::mCherry (compare to N2 wt). **g**, Width of the point-spread function of membrane-associated fluorophores for GFP, as well as mCherry (**h**). Left side, fluorescence intensity profile of the 40 pixel band (8.7 μm) around the membrane (insert, original image). Right side, individual fluorescent intensity profile (black) and fit (blue), as explained above, with $\sigma_g = 344$ nm for GFP and $\sigma_g = 306$ nm for mCherry. Measurement of the ensemble-averaged cytoplasmic and membrane bound total amount of NMY-2, PAR-2 and PAR-6, for the following conditions **i**, *mlc-4* RNAi (N=8), **j**, *par-2* and *par-6* double RNAi (N=8 for NMY-2, N=10 for PAR-2 and PAR-6), **l**, PAR-2 MT- mutant (N=6 for NMY-2, N=9 for PAR-2 and PAR-6), **m**, unperturbed condition (N=8 for NMY-2, N=6 for PAR-2 and PAR-6). **k**, Individual point spread function of one 100 nm TetraSpeck fluorescent bead. Red and black: fluorescence intensity along the x and y direction. Blue: fluorescence intensity along the z direction. Open circles show the data, the solid line represents a gaussian fit to the data, yielding σ_x = 0.191 μm in x, σ_y = 0.173 μm in y and σ_z = 0.46 μm in z. **n**, The sum of the membrane-bound and cytoplasmic PAR-2 and PAR-6 amount in protein number, for the unperturbed condition (N=6) and *par-6* RNAi (N=6). **o**, The membrane-bound amount of PAR-2 and PAR-6 in protein number, for the unperturbed condition (N=6) and *par-6* RNAi (N=6). **p**, The sum of the membrane-bound and cytoplasmic PAR-2 and PAR-6 amount in protein number, for the unperturbed condition (N=6) and *par-2* and *par-6* double RNAi (N=10). **q**, The membrane-bound amount of PAR-2 and PAR-6 in protein number, for the unperturbed condition (N=6) and *par-2* and *par-6* RNAi (N=10). See section 'Determining total protein amounts, Methods' for details.

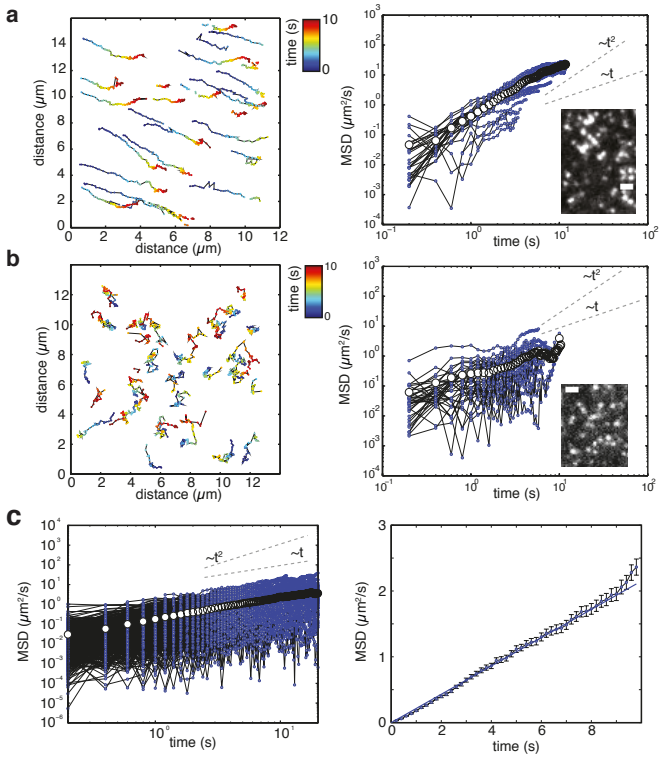

Fig. S4 – Measuring the NMY-2 diffusion constant. **a**, Trajectories and mean squared displacement of NMY-2 during the flow phase, for an individual movie. Blue dots: individual tracks, white dots: average. (Scale bar: 1 μm) **b**, Trajectories and mean squared displacement of NMY-2 during *ect-2* RNAi, for an individual movie. Blue dots: individual tracks, white dots: average. (Scale bar: 1 μm) **c**, Ensemble-averaged mean squared displacement of 7 movies, during *ect-2* RNAi. We restricted our analysis to tracks with a minimum length of 3 seconds (N=657 tracks). Blue dots: individual tracks, white dots: average. Fitting a mean squared displacement, linear in time resulted in D_M= 0.054 $\mu m^{2-1} \pm 0.081\ \mu m^2 s^{-1}$.

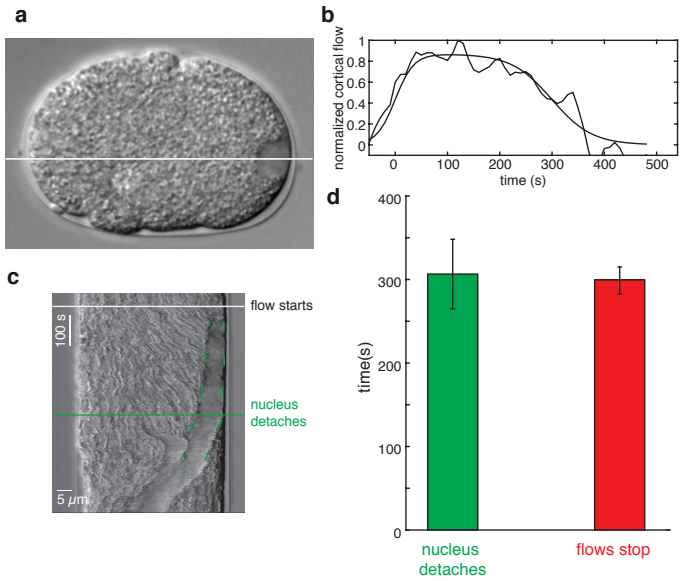

Fig. S5 – The actomyosin cue becomes inactive when the centrosome detaches from the cortex. **a**, DIC image of a one cell *C. elegans* embryo. The white line indicates the representative position of the kymograph, shown in **c**, Kymograph of DIC images, indicating two events: 1) Start of cytoplasmic flows, 2) Detachment of the male pronucleus from the cell membrane. This separates the centrosome, which is physically attached to the male pronucleus, from the actomyosin cortex. **b**, Temporal profile of the normalized average cortical flow profile in the posterior domain (between -30 µm to 30 µm, with respect to the posterior pole) on a data-set where DIC movies and NMY-2 fluorescence was measured in parallel (N=8). To extract the cessation of flows, we fitted this temporal profile with $f(t) = \frac{1}{2}\left[\tanh(\frac{t}{\tau_{\text{on}}}) - \tanh(\frac{t-T_{\text{stop}}}{\tau_{\text{off}}})\right]$, where T_{stop} gives the time when flows stop. **d**, Quantification of the average time between the start of flows and the moment where the nucleus detaches from the cell membrane as well as time between the start of flows and the cessation of cytoplasmic flows, extracted from the same data set (N=8). Error bars: 95% confidence interval.

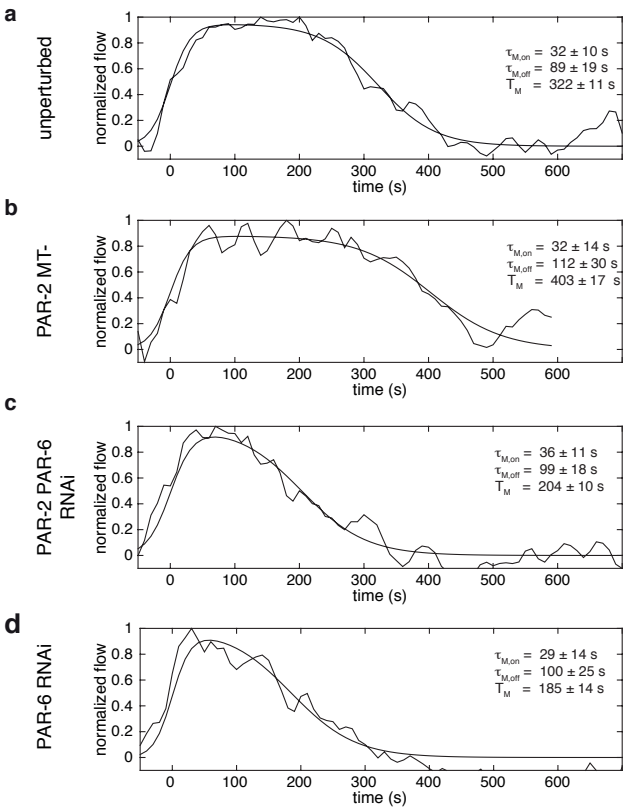

Fig. S6 – Temporal profile of normalized, averaged amplitude of cortical flows, induced by the the actomyosin cue. **a**, unperturbed condition (N=12), **b**, PAR-2 MT- (N=9), **c**, *par-2* and *par-6* double RNAi (N=10), **d**, *par-6* RNAi (N=11). For all conditions, the absolute value of the cortical flow field was averaged in space, over the posterior domain (between -30 µm to 30 µm, with respect to the posterior pole). We fitted the temporal profile with $f_M(t) = \frac{1}{2}\left[\tanh(\frac{t}{\tau_{M,\mathrm{on}}}) - \tanh(\frac{t-T_M}{\tau_{M,\mathrm{off}}})\right]$, where the results are summarized in Supplementary Table S3 . Errors represent the 95% confidence interval.

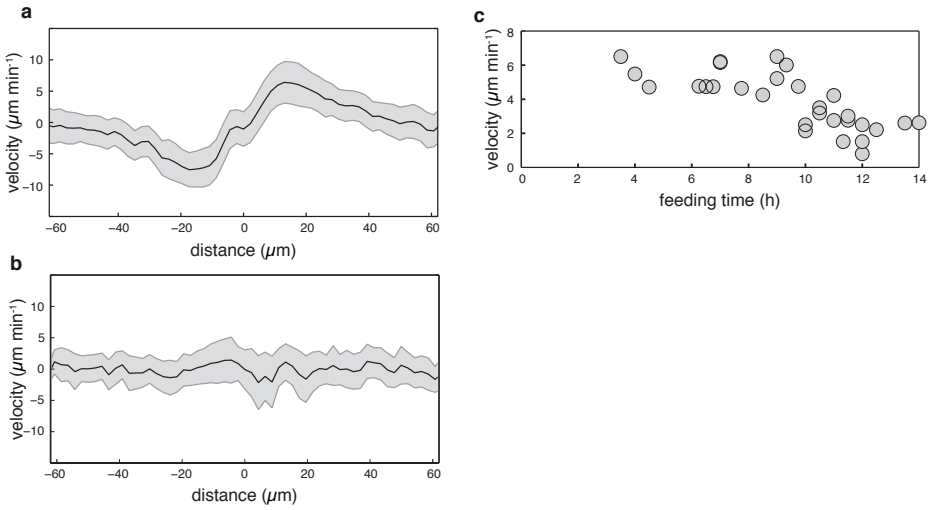

Fig. S7 – Actomyosin flows during *mlc-4* RNAi. **a**, Average of the cortical flow over 12 embryos and 100 s, for the unperturbed condition. **b**, Average of the cortical flow over 7 embryos and 100 s, for *mlc-4* RNAi. Error band represents the 95% confidence interval. **c**, Dependence of the cortical flow velocity on the *mlc-4* RNAi feeding time. We determined cortical flow velocities for *mlc-4* RNAi by investigating the displacement-field of yolk granules adjacent to the actomyosin cortex, using the freely available PIVlab MATLAB algorithm (*27*). 2D velocity fields were projected onto the anterior-posterior axis by dividing the embryo into 18 bins along the anterior-posterior axis, and by spatially averaging the x-component or the y-component of velocity along each bin in a single frame. The average velocity in each bin was then averaged over time across the entire flow period. The peak velocity was then determined as the maximum of the spatial flow profile.

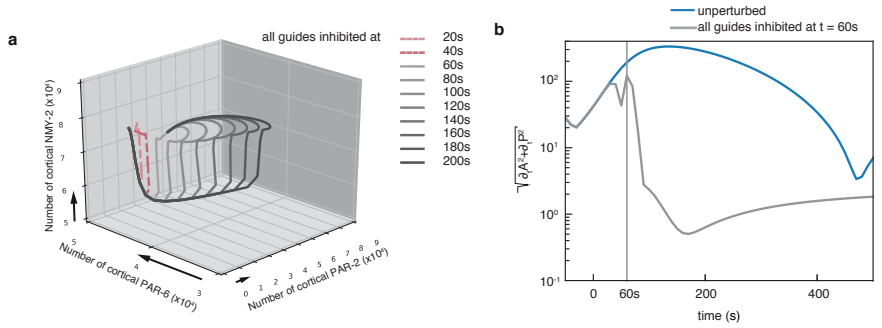

Fig. S8 – Characterizing the transition point. textbfa, Response of the PAR - actomyosin self-organization system upon cue inhibition at various time-points. Numerical simulation of the PAR - actomyosin self-organization system, shown analogous to Fig. 4a, main text, using unperturbed-condition parameters, when all three cues are disabled at time-points between 20s and 200 s. Note that for 20s and 40s, the system relaxes back to the initial state (homogeneous), while afterwards, it relaxes to the patterned polarity domain state. **b**, Speed of the PAR system, defined by $\sqrt{(\partial_t \mathrm{N_A})^2 + (\partial_t \mathrm{N_P})^2}$. Here $\mathrm{N_A}$ and $\mathrm{N_P}$ denote the number of cortical PAR-6 and PAR-2, respectively (see Fig. 4a, main text). The unperturbed condition (blue) is compared to the trajectory, for which all cues are disabled after the cues operate for 60s, just beyond the transition point.

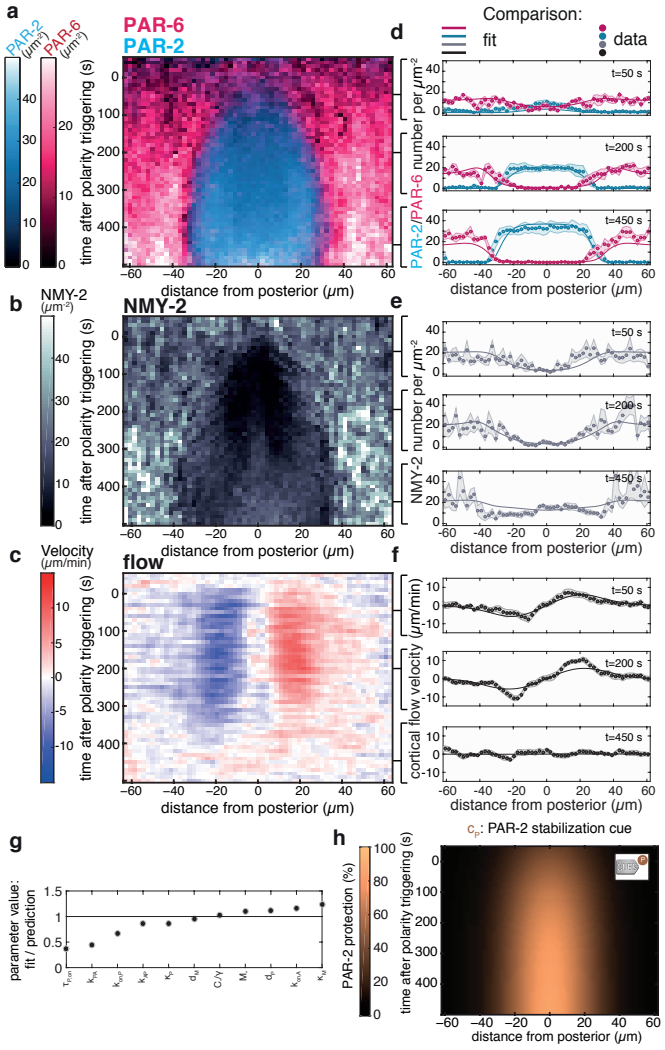

Fig. S9 – Fitting the unperturbed condition. a-c, Ensemble averaged concentrations of PAR-2::GFP, PAR-6::mCherry (N=6, both) and NMY-2::GFP (N=8) as well as the NMY-2 flow field (N=12) during polarity establishment, for the unperturbed condition. **d-f**, Comparison of the experimental PAR-2, PAR-6 and NMY-2 concentration profiles as well as flow fields (dots, shaded regions represent standard error of the mean) with the fit of the theory of guided mechanochemical self-organization, displayed at t=50s, 200s and 450s (solid lines), for the unperturbed condition (Supplementary Video 5). **g**, Ratio of the parameter values that have been fitted and the parameter values used for the prediction (Fig. 3k-m, main text). **h**, Spatiotemporal profile of the PAR-2 stabilization cue, obtained by fitting the unperturbed condition.

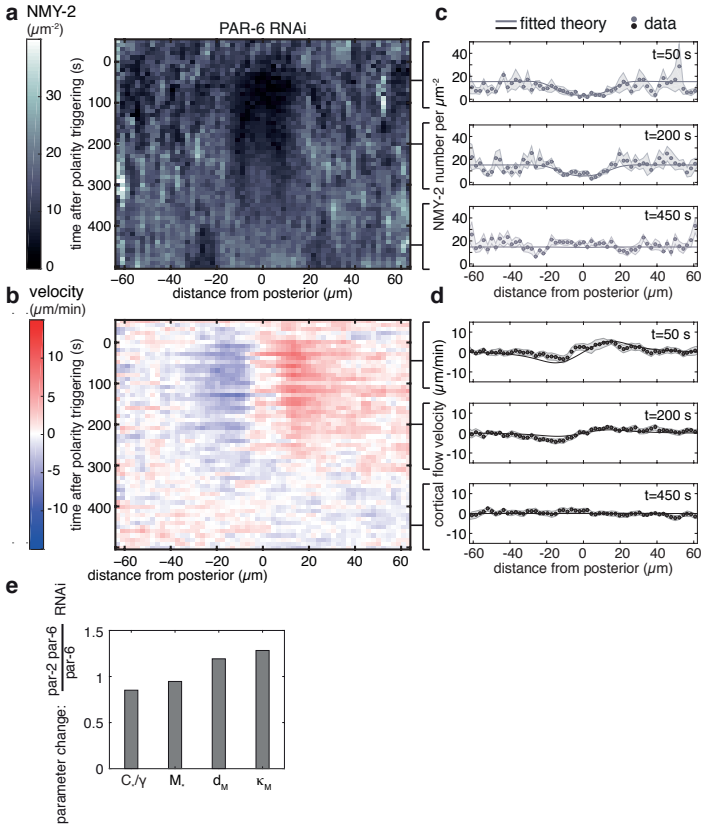

Fig. S10 – Quantifying the effect of the actomyosin cue on the NMY-2 system in isolation, during *par-6* RNAi . **a**, Kymograph of the ensemble averaged concentration field of NMY-2 (N=7) during *par-6* RNAi. **b**, Kymograph of the ensemble averaged flow field of NMY-2 (N=11) during *par-6* RNAi. **c**, Comparison of the experimental NMY-2 concentration profiles with the best fit, displayed at t=50s, 200s and 450s. **d**, Comparison of the experimental flow profile with the best fit, displayed at t=50s, 200s and 450s. **e**, Ratio of the parameters: C_*/γ (Contractility), M_* (Contractility saturation), d_M (width, myosin removal cue), κ_M (strength, myosin removal cue) from the *par-2* and *par-6* double RNAi condition over the *par-6* RNAi condition.

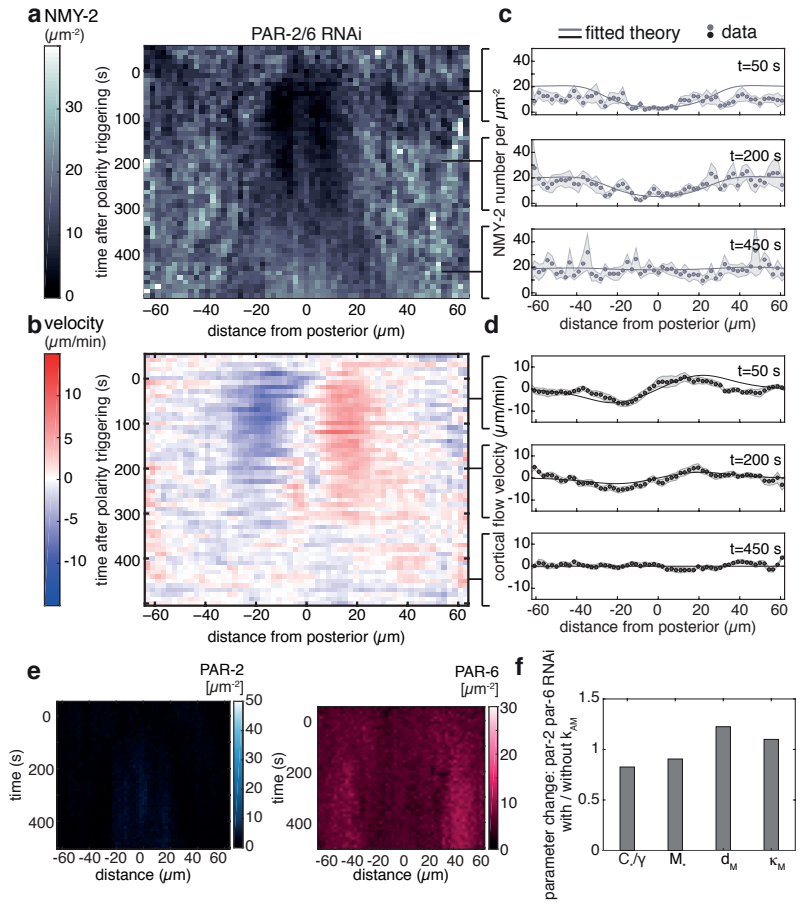

Fig. S11 – Fitting the NMY-2 - flow system, during *par-2* and *par-6* double RNAi, while also considering the experimentally measured PAR membrane concentrations. **a**, Kymograph of the ensemble averaged concentration field of NMY-2 (N=8) during *par-2* and *par-6* double RNAi. **b**, Kymograph of the ensemble averaged flow field of NMY-2 (N=10) during *par-2* and *par-6* double RNAi. **c,d**, Comparison of the experimental NMY-2 concentration profiles and flow fields with the best fit, displayed at t=50s, 200s and 450s. This fitting procedure explicitly considered the experimentally measured PAR-2 and PAR-6 concentrations (**e**). **f**, Ratio of the parameters: C_*/γ (Contractility), M_* (Contractility saturation), d_M (width, myosin removal cue), κ_M (strength, myosin removal cue) from the *par-2* and *par-6* double RNAi condition, obtained while ignoring the PAR concentrations over the best fit that explicitly considers the experimentally measured PAR-2 and PAR-6 concentration (**e**).

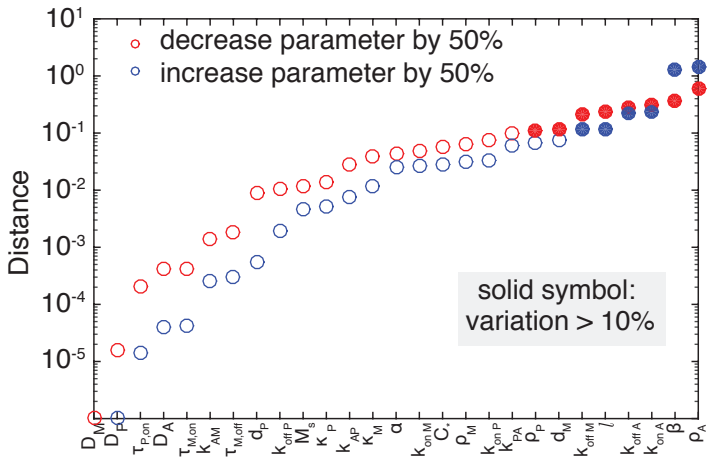

Fig. S12 – Parameter sensitivity analysis. Displayed is the distance measure (Supplementary Equation 50) between the unperturbed-condition solution and the model solution, where one parameter value is either increased or decreased by 50%. Solid symbols: variation of the solution is bigger than 10%.

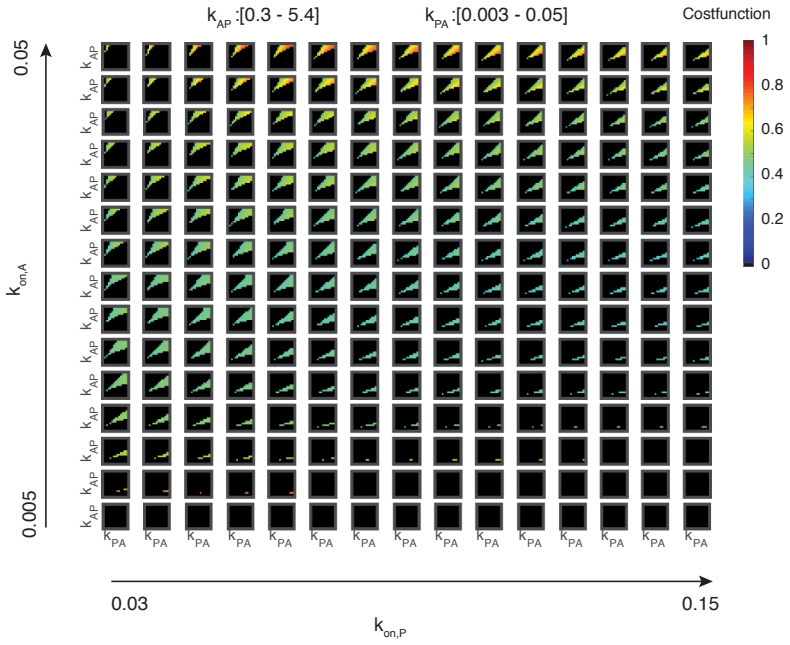

Fig. S13 – Cost-function when comparing the experimental *mlc-4* RNAi condition with the theoretical solutions. Four parameters were varied. Each box shows the cost-function against k_{AP} and k_{PA}, with a range between 0.3 - 5.4 μm^2 and 0.003 - 0.05 $\mu m^4 s^{-1}$, respectively. Boxes with increasing row number show the cost-function evaluated at increasing values of $k_{on,A}$, while increasing column numbers show values of increased $k_{on,P}$. $k_{on,A}$ was varied between 0.005 - 0.05 $\mu m s^{-1}$ and $k_{on,P}$ was varied between 0.03 - 0.15 $\mu m s^{-1}$. The cost-function is evaluated according to Supplementary Equation 48. Black regions indicate the parameter space where either the homogeneous A high state is unstable or the PAR reaction chemistry does not support multistability, or both.

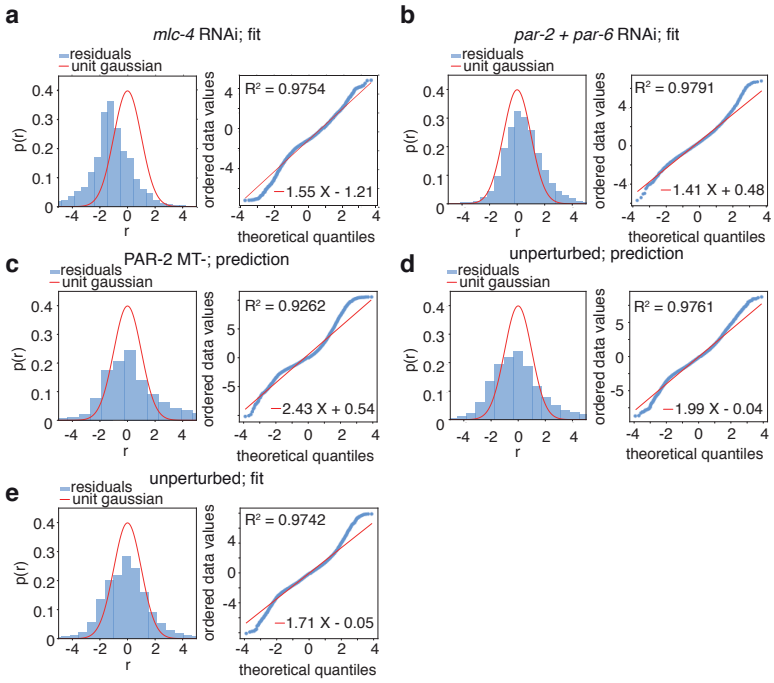

Fig. S14 – Quantifying the goodness of the fit / prediction for five conditions. **a**, *mlc-4* RNAi, **b**, *par-2* + *par-6* RNAi, **c**, PAR-2 MT- (*15*) prediction, **d**, unperturbed prediction, **e**, unperturbed, while fitting unknown parameters (Supplementary Fig. 9). We calculated the residuals between the experimental and theoretical results, which were normalized by the experimental standard error of the mean. For perfect agreement, this should yield a gaussian distribution with zero mean and unit width. To determine how well the experimental distribution agrees with the such a gaussian distribution, we also show quantile plots, which should, for perfect agreement, show a line with zero intercept and slope 1 (see Supplemental Information, section 2.6.1).

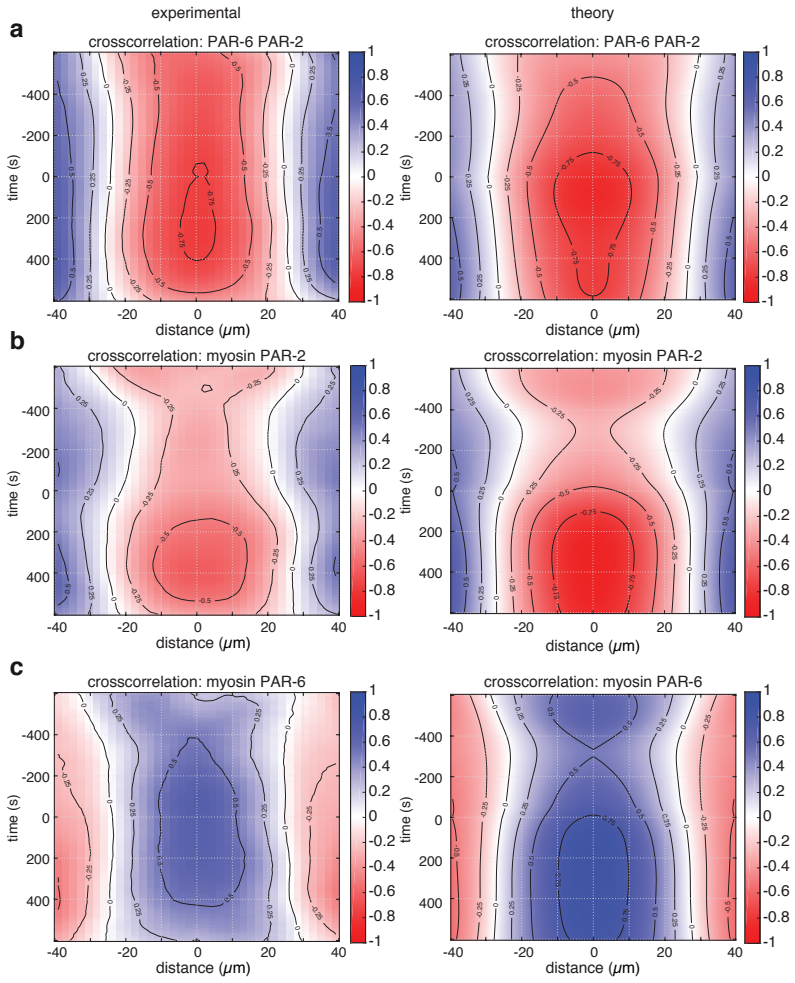

Fig. S15 – Normalized crosscorrelation between the PAR-2, PAR-6, and myosin concentration fields a, Comparison of the crosscorrelation between the ensemble-averaged experimental and theoretical concentration fields of PAR-2 and PAR-6 (N=6 for both). **b**, Comparison of the crosscorrelation between the ensemble-averaged experimental and theoretical concentration fields of myosin (N=8) and PAR-2 (N=6). **c**, Comparison of the crosscorrelation between the ensemble-averaged experimental and theoretical concentration fields of myosin (N=8) and PAR-6 (N=6) (see Supplemental Discussion).